WKB analysis of edge states in graphene in a strong magnetic field

Pierre Delplace and Gilles Montambaux
Laboratoire de Physique des Solides, CNRS UMR 8502, Université Paris-Sud, 91405 Orsay, France
(Received 28 July 2010; revised manuscript received 7 October 2010; published 9 November 2010)

We investigate the fine structure of the edge states energy spectrum for zigzag and armchair ribbons of graphene in a strong magnetic field. At low energy, the spectra can be described by an effective Schrödinger Hamiltonian with a double well potential, symmetric in the zigzag case and asymmetric in the armchair case. We develop a semiclassical formalism based on the WKB approximation to calculate analytically the energy spectrum for the two types of edges, including regions which were not studied earlier. Our results are in very good quantitative agreement with numerical calculations. This approach leads to a qualitative description of the spectra in terms of the quantization of unusual classical orbits in the real space.

DOI: 10.1103/PhysRevB.82.205412 PACS number(s): 73.22.Pr, 03.65.Sq, 73.43.−f

I. INTRODUCTION

The fascinating properties of graphene originate from its perfect two-dimensional (2D) character and from its unusual electronic structure where valence and conduction bands touch at two inequivalent points of reciprocal space. In the vicinity of these two points, the dispersion relation is linear and charge carriers behave as massless Dirac fermions[1] with striking consequences on the electronic properties, like the unusual 2D quantum Hall effect.[2,3] Recent studies have also addressed electronic properties of confined graphene structures such as dots, rings, or nanoribbons. In particular, nanoribbons have been suggested as potential candidates for replacing electronic components in future nanoelectronic and nanospintronic devices.[4,5] In that perspective, the role of edge states is essential. In the absence of magnetic field, edge states can emerge for particular types of edges.[6,7] Such localized electronic states can be described analytically at low energy by using the Dirac equation with the appropriate boundary conditions.[8] More recent theoretical works have investigated the metallic nature of such edge states by considering staggered on-site potentials,[9] surface perturbations,[10] spin-orbit coupling,[11] edge doping,[12] and sophisticated terminations of the honeycomb lattice.[13–15] Experimental efforts have been performed to observe different natures of edges[16–18] and study charge transport in ribbons.[19,20]

This paper deals with the structure of edge states in a strong magnetic field, a problem which has been the subject of recent interest.[21–23] Although this problem is somehow reminiscent of the case of usual 2D electrons,[24,25] it is much richer since here charge carriers are massless particles and the structure of the edge states depends on the nature of the edges, the so-called zigzag and armchair edges. These two types of edges can be described at low energy by an effective Schrödinger Hamiltonian with a harmonic potential.[21,23] In the zigzag case, this potential is similar to the one of the usual integer quantum Hall problem,[24] whereas in the armchair case, the potential presents a specific asymmetry.[21,23] Moreover, these edge states have been recently investigated numerically in graphene rings,[26] and in graphene ribbons by considering an anisotropic hopping parameter,[27] or by taking account for a possible quantum Hall ferromagnetism.[28]

However, the energy dependence of the Landau levels when approaching the edges has only been discussed briefly. The goal of this paper is to investigate in details the fine structure of the edge states energy spectrum for zigzag and armchair ribbons and provide a complete *quantitative analytical* description within the WKB approximation. The paper is organized as follows: in Sec. II, we recall and discuss in details the tight-binding spectra for zigzag and armchair ribbons with and without magnetic field. When a field is applied, we point out peculiar features of the edge states which we describe analytically in the rest of the paper. Following the procedure suggested in previous works,[21,23] we derive in Sec. III a simple effective Hamiltonian (essentially the squared Dirac Hamiltonian) with a potential depending on the boundary conditions. Then, in Sec. IV, we present a semiclassical framework to calculate analytically the low-energy spectra. Two methods are used: the first one is based on the Bohr-Sommerfeld quantization (BSQ) of the action and leads to a simple qualitative picture in terms of classical skipping orbits in Sec. V. However, this method does not properly describe the case where the classical cyclotron radius is on the order of the distance to the edge. Therefore, we develop a more sophisticated semiclassical approach, based on the WKB approximation, that leads to analytical quantitative results in agreement with numerical calculations. The details of this approach are given in the Appendix A. We conclude in Sec. VII.

II. TIGHT-BINDING SPECTRUM

A. Zero magnetic field

We briefly recall the band structure of infinite graphene ribbons within the tight-binding picture. For that purpose, we first consider the Hamiltonian H of an infinite 2D sheet of graphene, and we use the Bloch theorem in both x and y directions. As the honeycomb lattice has two carbon atoms per cell (that we call A and B, see Fig. 1), the Bloch wave function is written as

$$|\Psi_{\vec{k}}\rangle = \sum_j e^{i\vec{k}\vec{R}_j}[\Psi_A|A_j\rangle + \Psi_B|B_j\rangle], \tag{1}$$

where $\vec{R}_j$ are the vectors of the triangular Bravais lattice. Then, within the tight-binding model, the Hamiltonian is written as

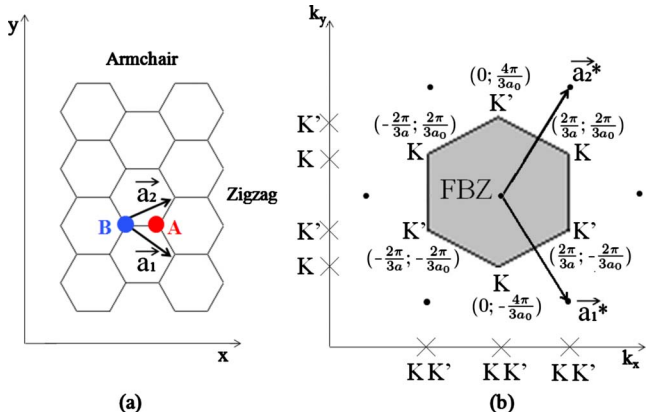

FIG. 1. (Color online) (a) Sheet of graphene with zigzag and armchair edges. (b) The black dots represent the nodes of the triangular reciprocal lattice whose $\vec{a}_1^*$ and $\vec{a}_2^*$ are the basis vectors. The Dirac points $\vec{K}$ and $\vec{K}'$ are located at the corners of the FBZ. The projections of the $\vec{K}$ and $\vec{K}'$ points on the k_x and k_y axes have been represented by crosses.

$$H = t\begin{pmatrix} 0 & f(\vec{k}) \\ f^*(\vec{k}) & 0 \end{pmatrix} \tag{2}$$

in the basis of the two sublattices (Ψ_A, Ψ_B), where t is the hopping parameter between nearest neighbors and with

$$f(\vec{k}) = -1 - \exp(i\vec{k}\cdot\vec{a}_1) - \exp(i\vec{k}\cdot\vec{a}_2), \tag{3}$$

where $\vec{a}_1$ and $\vec{a}_2$ are the basis vectors of the triangular Bravais lattice with $\|\vec{a}_1\| = \|\vec{a}_2\| \equiv a_0$. The lattice parameter a_0 is related to the carbon-carbon distance $a = 0.142$ nm by $a_0 = \sqrt{3}a$. The dispersion relation given by $\epsilon(\vec{k}) = \pm t|f(\vec{k})|$ [see Fig. 2(a)] consists in two bands which touch at the corners of the first Brillouin zone (FBZ). The positions of these points are given by the condition $f(\vec{K}) = 0$, that is,

$$\vec{K} = \frac{1}{3}(\vec{a}_1^* - \vec{a}_2^*) \quad \vec{K}' = -\frac{1}{3}(\vec{a}_1^* - \vec{a}_2^*),$$

where $\vec{a}_1^*$ and $\vec{a}_2^*$ are the basis vectors of the reciprocal lattice. The spectrum is linear near these points. The choices of the unit cell and of the axes are illustrated in Fig. 1(a). The positions of the so-called $\vec{K}$ and $\vec{K}'$ Dirac points are shown in Fig. 1(b), where we have also indicated their projections onto the axis k_x and k_y.

We consider now infinite ribbons with either zigzag or armchair edges. In these finite geometries, the Bloch theorem can be used only along the infinite direction, and the boundary condition along the finite direction yields a finite number of bands. These bands, computed in the tight-binding model, are displayed in Figs. 2(d) and 2(e). It is seen that the spectra of these ribbons correspond to the projection of the 2D spectrum along the k_x axis (armchair edge) or the k_y axis (zigzag edge). The projected points $\vec{K}$ and $\vec{K}'$ coincide in the armchair case but they do not in the zigzag case. This remark illustrates the fact that for the armchair case, the two valleys are admixed by the boundary condition as we will discuss later. Finally, note that the flat level between the two points $\vec{K}$ and $\vec{K}'$ for zigzag edge is not captured by the projection of the bulk result. This zero energy state is localized near the edges and its existence depends on the boundary conditions.[7,8,29] This edge state exists without any magnetic field.

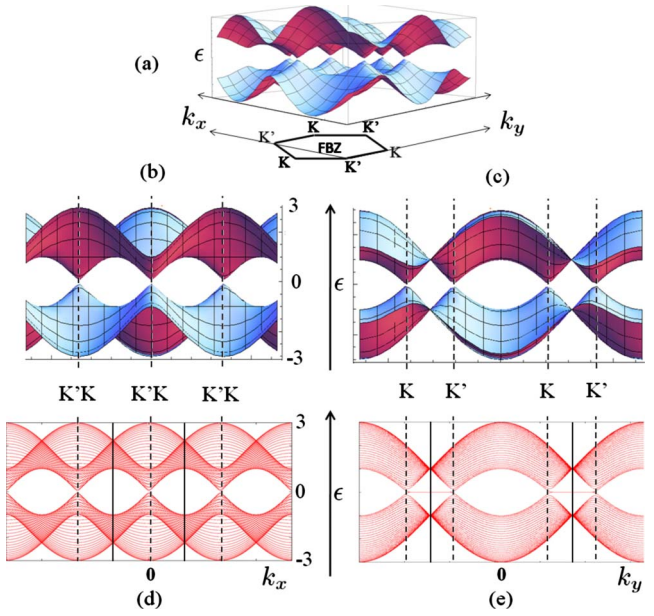

FIG. 2. (Color online) (a) Energy spectrum $\epsilon(\vec{k})$ of an infinite sheet of graphene. Projection of this spectrum (b) along the k_y axis onto the plane (ϵ, k_x) and (c) along the k_x axis onto the plane (ϵ, k_y). Band structure (d) for an infinite armchair ribbon and (e) for a zigzag ribbon. Their widths are $L = 49a_0/2$ for the armchair ribbon and $L = 49\sqrt{3}a_0/2$ for the zigzag ribbon. The positions of the $\vec{K}$ and $\vec{K}'$ points are represented by dashed vertical lines and the one-dimensional FBZ is delimited by continuous vertical lines. The energies are given in units of the hopping parameter t.

From now on, we define the geometry of the armchair and zigzag ribbons as shown in Fig. 3: the ribbon is infinite along the y direction and it has a finite width L in the x direction.

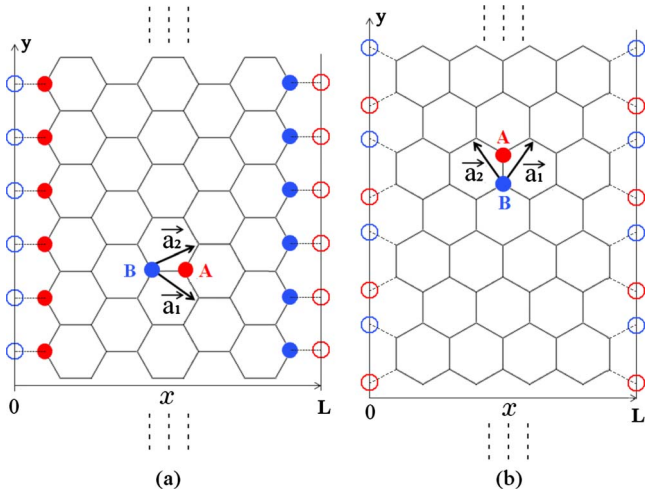

FIG. 3. (Color online) Graphene ribbons of width L with (a) zigzag edges and (b) armchair edges. We consider the y direction as infinite. The circles represent empty sites and define the edges.

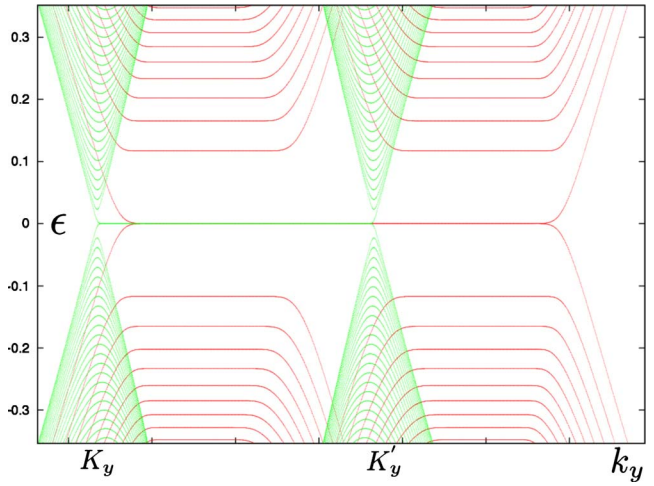

FIG. 4. (Color online) Tight-binding spectrum at low energy for a zigzag ribbon with (red) and without (green) magnetic field. The magnetic flux is $\phi=0.00126\phi_0$ and the width is $L=199\sqrt{3}a_0/2$.

Within this convention, we have $K_y \neq K'_y$ for the zigzag ribbons and $K_y=K'_y$ for the armchair ones.

B. Perpendicular magnetic field

We now apply a perpendicular magnetic field $\vec{B}=-B\vec{e}_z$ on each type of ribbon and calculate numerically the band structure within the tight-binding model.[21] The finite width of the ribbons along the x axis leads us to work with the Landau gauge $A_y=-Bx$ and $A_x=0$. Because of the vector potential A_y, the hopping parameter t (taken as unity in the rest of the paper), takes a Aharonov-Bohm phase $t \rightarrow te^{i(2\pi/\Phi_0)\int d\vec{l}\cdot\vec{A}}$, where $\phi_0=h/e$ is the magnetic-flux quantum. We now study the low-energy spectrum for a given magnetic flux ϕ through an elementary plaquette. In Fig. 4, we show the low-energy tight-binding spectra for the zigzag ribbon with and without magnetic field in the same plot. The spectra for the armchair case are shown in Fig. 5. The zero-field cones are progressively transformed into flat Landau levels with the expected $\epsilon_n=\pm t\sqrt{2\pi\sqrt{3}n\phi/\phi_0}$ behavior.[30]

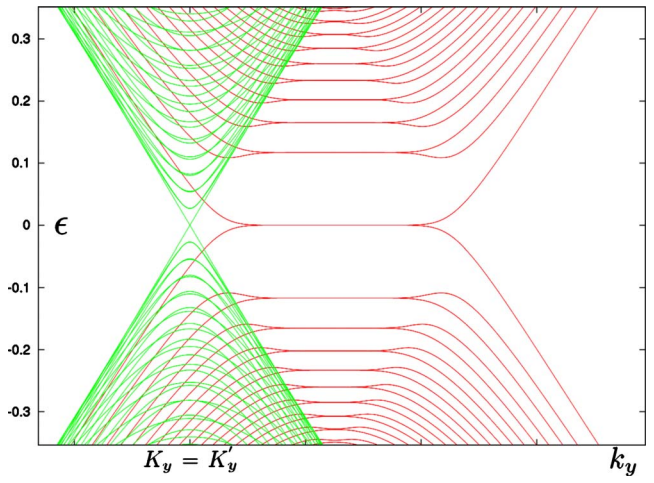

FIG. 5. (Color online) Tight-binding spectrum at low energy for an armchair ribbon with (red) and without (green) magnetic field. The magnetic flux is $\phi=0.00126\phi_0$ and the width is $L=199a_0/2$.

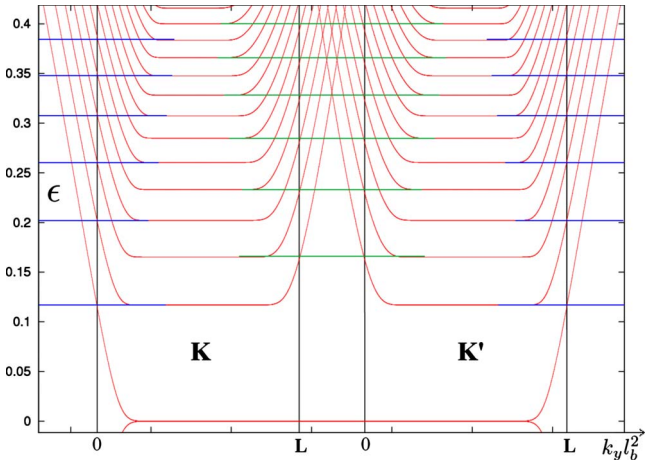

FIG. 6. (Color online) Tight-binding low-energy levels in the quantum Hall regime as a function of the position $k_y\ell_B^2$ along the x axis for a zigzag ribbon. The edges are represented by vertical black lines. Green and blue horizontal lines indicate the position of the bulk Landau levels for comparison with the position of the levels at the edges. Note the mirror symmetry of the spectrum between the two valleys $\vec{K}$ and $\vec{K}'$. The energy is given in units of t.

We now comment on several important features of these spectra which to our knowledge have not been discussed in the literature. Since in the chosen Landau gauge, a state k_y is centered at the position $k_y\ell_B^2$ along the x direction, where $\ell_B=\sqrt{\hbar/eB}$ is the magnetic length, the variation in the energy levels can be interpreted as a function of this position, as redrawn in Figs. 6 and 7. In these figures, we have indicated the position of the edges along the x direction, at low energy. Indeed, the position of one edge is fixed by the position of the Dirac points in zero field and the other edge is located at a distance $\Delta q_y=L/\ell_B^2$, where L is the width of the ribbon and where $q_y=k_y-K_y^{(\prime)}$. As the two valleys are not admixed in the zigzag case, this operation must be performed for both $\vec{K}$ and

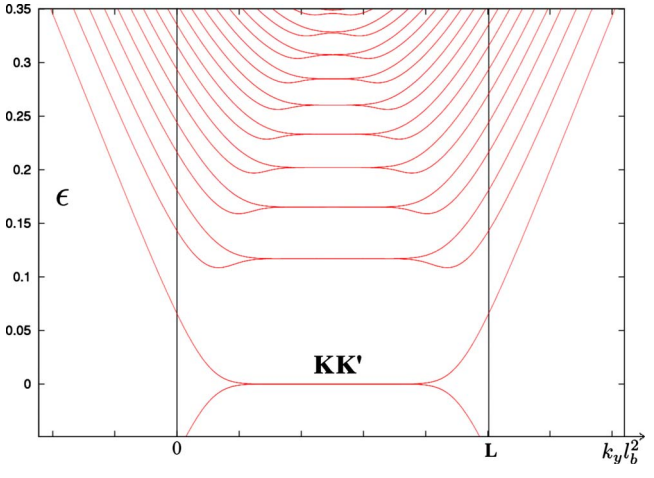

FIG. 7. (Color online) Tight-binding low-energy levels in the quantum Hall regime as a function of the position $k_y\ell_B^2$ for an armchair ribbon. The edges are represented by vertical black lines. The energy is given in units of t.

$\vec{K}'$ valleys, as seen in Fig. 6. Therefore, it is clear that the dispersive character of the levels corresponds to the edge states, as first discussed by Halperin in the context of the integer quantum Hall effect of massive particles in two-dimensional gases.[24] However, the band structure for graphene is more complex and depends on the type of edge as we discuss now. For the zigzag edge, we first emphasize that, inside a given valley, *the spectrum is not symmetric*: the energy levels are not identical on left and right sides. Moreover, exactly at the left and right edges, the energy levels ϵ^{edge} take peculiar values: they alternatively take the value of higher bulk Landau levels ϵ^{bulk}. This correspondence is displayed by horizontal color lines in Fig. 6. More precisely, for the $\vec{K}$ valley, we have the relation $\epsilon_n^{edge}=\epsilon_{2n+1}^{bulk}$ with $n\geq 0$ (horizontal blue lines) on the left edge whereas we have $\epsilon_n^{edge}=\epsilon_{2n}^{bulk}$ (horizontal green lines) with $n>0$ for the right edge. In addition, we have the same structure in the $\vec{K}'$ valley, provided the role of the two edges is permuted. This remarkable distribution of the edge states will be explained in Sec. IV C. The armchair case, in Fig. 7, is quite different. Each Landau level is doubly degenerate, a direct consequence of the valley admixing. The degeneracy lifting takes place close to the edge with a nonmonotonous behavior for one every two levels that will be explained in Sec. IV C. In the following we present a qualitative and quantitative description of these spectra within a semiclassical analytical approach.

III. LOW-ENERGY EFFECTIVE HAMILTONIAN

A. Bulk Hamiltonian

At low energy, Hamiltonian (2) can be linearized around the two Dirac points $\vec{K}$ and $\vec{K}'$. Expanding $\vec{k}$ as $\vec{k}=\vec{K}^{(\prime)}+\vec{q}$ in each valley, the tight-binding Hamiltonian is then replaced by a 4×4 linearized Dirac-type Hamiltonian,

$$\hat{H}=\gamma a_0\begin{pmatrix} 0 & i\hat{q}_x-\hat{q}_y & 0 & 0 \\ -i\hat{q}_x-\hat{q}_y & 0 & 0 & 0 \\ 0 & 0 & 0 & i\hat{q}_x+\hat{q}_y \\ 0 & 0 & -i\hat{q}_x+\hat{q}_y & 0 \end{pmatrix}, \tag{4}$$

which describes the two uncoupled valleys in the basis $(\varphi_A,\varphi_B,\varphi'_A,\varphi'_B)$, where $\gamma=\frac{\sqrt{3}}{2}t$ and a_0 is the lattice spacing. The eigenfunctions $\Psi^{\pm}$ can be expressed as the superposition of the contributions of the two valleys so that we can write

$$\Psi^{\pm}(\vec{r})=e^{i\vec{K}\vec{r}}\begin{pmatrix}\varphi_A(\vec{r})\\ \varphi_B(\vec{r})\end{pmatrix}\pm e^{i\vec{K}'\vec{r}}\begin{pmatrix}\varphi'_A(\vec{r})\\ \varphi'_B(\vec{r})\end{pmatrix}. \tag{5}$$

In the magnetic field $\vec{B}=-B\vec{e}_z$, and within the Landau gauge $A_y=-Bx$, we perform the Peierls substitution $\hat{q}_y\to\hat{q}_y+e\hat{A}_y=\hat{q}_y-eB\hat{x}$. Then we introduce the dimensionless variables $\hat{x}/\ell_B\to\hat{x}$ and $x_c=q_y\ell_B$. Since $\hat{q}_x=-i\partial_x$, the Hamiltonian in a magnetic field reads

$$\hat{H}=\frac{v_F}{\ell_B}\times\begin{pmatrix} 0 & \partial_x+x-x_c & 0 & 0 \\ -\partial_x+x-x_c & 0 & 0 & 0 \\ 0 & 0 & 0 & \partial_x-(x-x_c) \\ 0 & 0 & -\partial_x-(x-x_c) & 0 \end{pmatrix}, \tag{6}$$

where $v_F=\gamma a_0$ is the Fermi velocity. Next, it is useful to work with the squared Hamiltonian $\hat{H}^2$ which is diagonal. We introduce the dimensionless effective Hamiltonian $\mathcal{H}_{eff}$ as

$$\hat{H}^2=2\frac{v_F^2}{\ell_B^2}\mathcal{H}_{eff}, \tag{7}$$

which defines four effective Schrödinger equations,

$$\mathcal{H}_{eff}\Psi=E_n\Psi \tag{8}$$

with

$$\mathcal{H}_{eff}=-\frac{\mathbb{1}}{2}\partial_x^2+\begin{pmatrix} V_u(x) & 0 & 0 & 0 \\ 0 & V_d(x) & 0 & 0 \\ 0 & 0 & V_d(x) & 0 \\ 0 & 0 & 0 & V_u(x) \end{pmatrix}, \tag{9}$$

where the potentials $V_u(x)$ and $V_d(x)$ are given by

$$V_u(x)\equiv\frac{1}{2}(x-x_c)^2+\frac{1}{2}, \tag{10}$$

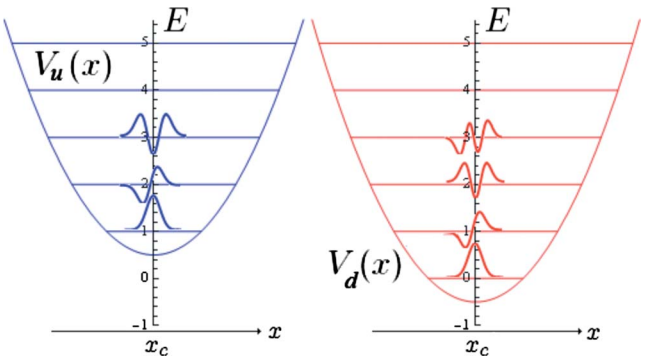

FIG. 8. (Color online) The harmonic potentials V_u and V_d of the effective Hamiltonian $\mathcal{H}_{eff}$. The eigenfunctions associated with the eigenvalues $E_n=n$ are the eigenfunctions of the harmonic oscillator, respectively, Φ_{n-1} and Φ_n.

$$V_d(x) \equiv \frac{1}{2}(x-x_c)^2 - \frac{1}{2} \tag{11}$$

and are displayed in Fig. 8. Thus, the effective Hamiltonian $\mathcal{H}_{eff}$ simply describes only two different harmonic oscillators. Because of the noncommutativity of the operators $\hat{x}$ and ∂_x, the two harmonic potentials $V_u(x)$ and $V_d(x)$ are shifted by one energy level. From Eqs. (8) and (9), one obtains two different Schrödinger equations, one with the potential $V_u(x)$ for φ_A and φ'_B, and the other one with the potential $V_d(x)$ for φ_B and φ'_A.

The eigenvalues ϵ_n of the original Hamiltonian (7) are obtained from the dimensionless eigenvalues E_n of the effective Hamiltonian $\mathcal{H}_{eff}$ as

$$\epsilon_n = \pm \frac{v_F}{\ell_B}\sqrt{2E_n}. \tag{12}$$

In the Landau gauge we have used, the wave function is a plane wave along the y direction and now reads

$$\Psi^{\pm}(\vec{r}) = \begin{pmatrix} \Psi_A^{\pm}(\vec{r}) \\ \Psi_B^{\pm}(\vec{r}) \end{pmatrix}$$

$$= e^{iq_y y}\left[e^{i\vec{K}\vec{r}}\begin{pmatrix} \varphi_A(x) \\ \varphi_B(x) \end{pmatrix} \pm e^{i\vec{K}'\vec{r}}\begin{pmatrix} \varphi'_A(x) \\ \varphi'_B(x) \end{pmatrix}\right]. \tag{13}$$

The eigenvalues $E_n=n$ are the Landau levels associated with the eigenfunctions of the harmonic oscillator $\{\Phi_n\}$ as follows:

$$\varphi_A = \Phi_{n-1} \quad \varphi'_A = \Phi_n,$$

$$\varphi_B = \Phi_n \quad \varphi'_B = -\Phi_{n-1}. \tag{14}$$

This is illustrated in Fig. 8. The effect of the edges is to modify the potentials [Eqs. (10) and (11)] and consequently the components $\varphi^{(\prime)}_{A/B}$ of the wave functions and the energy spectrum. These modifications depend on the nature of the edge which yields to specific boundary conditions. In the two following sections, we derive the effective Schrödinger equations for zigzag and armchair edges.

B. Zigzag edges

To treat the zigzag edges of a graphene ribbon, we first recall that all the atoms on one edge belong to the same sublattice, and therefore, all the atoms on the opposite edge necessarily belong to the other sublattice. As the ribbon is periodic in the y direction, we still write the low-energy wave functions $\Psi^{\pm}$ as in Eq. (13) but the components $\varphi^{(\prime)}_{A/B}$ are not the eigenfunctions of the harmonic oscillator anymore. As the left edge is only made of A sites (see Fig. 3), the wave function on the B sites vanishes for $x=0$, i.e., $\Psi_B^{\pm}(x=0,y)=0$. The situation is identical on the right edge at $x=L$ for the A sublattice: $\Psi_A^{\pm}(x=L,y)=0$. As a consequence, we have the boundary conditions,

$$\varphi_A(L)=0 \quad \varphi'_A(L)=0,$$

$$\varphi_B(0)=0 \quad \varphi'_B(0)=0. \tag{15}$$

These boundary conditions do not admix the valleys which can still be described separately, as in the bulk system. Consequently, with the zigzag boundary conditions, we have four independent Schrödinger equations, one for each valley and for each sublattice, with four independent potentials $V_A(x)$, $V_B(x)$, $V'_A(x)$, and $V'_B(x)$. Such boundary conditions can be accounted for by an infinite potential barrier either at $x=0$ or at $x=L$, according to the sublattice and the valley. Namely, the potentials $V_B(x)$ and $V'_B(x)$ are harmonic potentials that have to be cut in $x=0$ whereas the potentials $V_A(x)$ and $V'_A(x)$ have to be cut in $x=L$. Since the four edge problems are quite similar, we focus on the case of the right edge for the $\vec{K}$ valley. Thus, the potential $V_A(x)$ reads

$$V_A(x) = \begin{cases} V_u(x) & \text{for } x < L \\ \infty & \text{for } x > L \end{cases} \tag{16}$$

and is plotted in Fig. 9. Similarly, one can define $V'_A(x)$, $V_B(x)$, and $V'_B(x)$. As a matter of fact, the problem of a harmonic well with an infinite potential barrier (Fig. 9) is identical to the problem of a double symmetric harmonic well (Fig. 10), provided we only keep, in the latter, the eigenenergies associated with the eigenstates that vanish on the edge, that are the antisymmetric states. The interest of considering such a double symmetric well is that, as we will see in Sec. III C, both zigzag and armchair edges can be described by double harmonic wells, the difference being an energy shift between the two wells in the armchair case. We illustrate in Fig. 10 the double symmetric potential $V_A(x)$ we finally consider in the effective Schrödinger equation for the right zigzag edge and the $\vec{K}$ valley, that is,

$$\left[-\frac{1}{2}\partial_x^2 + V_A(x)\right]\Phi_{AS}(x) = E_n^{AS}(x_c)\Phi_{AS}(x), \tag{17}$$

$$V_A(x) = \frac{1}{2}(|x|+x_c)^2 + \frac{1}{2}. \tag{18}$$

The index AS refers to the antisymmetric solutions and we have performed the translations $x-L\to x$ and $x_c-L\to x_c$ so that the right edge is now located in $x=0$. The eigenenergies $E_n^{AS}(x_c)$ are calculated analytically within a WKB treatment

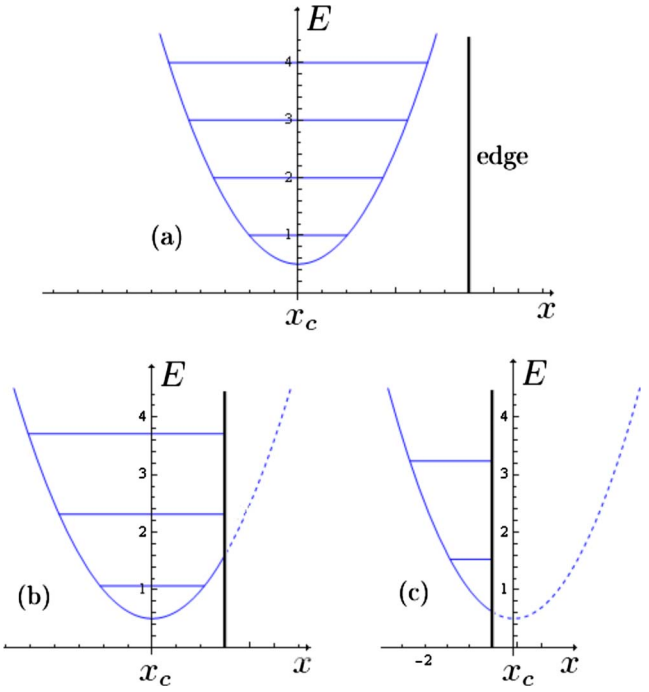

FIG. 9. (Color online) Potential $V_A(x)$ that describes the right edge in the $\vec{K}$ valley of a zigzag nanoribbon for the $\mathcal{H}_{eff}$ problem. The edge is modelized by an infinite potentia barrier.

introduced in Sec. IV. The detailed calculations are explained in the Appendix A.

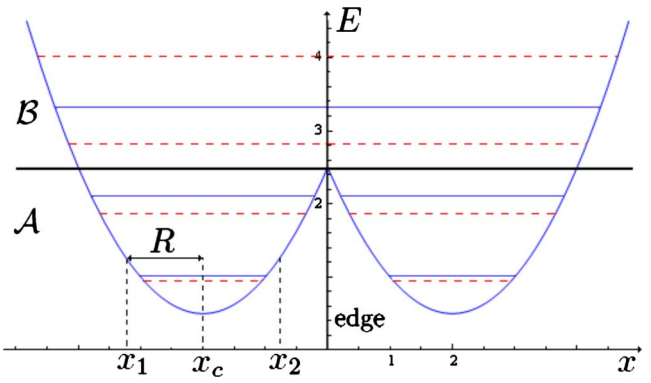

FIG. 10. (Color online) Double symmetric harmonic potential with $x_c=L-2$. We show the eigenenergies obtained within the WKB approximation. The higher energy levels (blue continuous lines) are the antisymmetric solutions. They are the same than those of a harmonic well cut by an infinite potential barrier (Fig. 9). For completion we have indicated the energies of the symmetric solutions (dashed red lines) which are not considered here. The two regions $\mathcal{A}$ and $\mathcal{B}$ and the cyclotron radius R are defined in Sec. IV.

C. Armchair edges

We now consider the case of an armchair ribbon as displayed in Fig. 3(b). The corresponding low-energy Hamiltonian is obtained from Eq. (4) by the substitution $q_y \to -q_x$ and $q_x \to q_y$. By keeping the same gauge $A_y=-Bx$ as above, the Hamiltonian in the presence of a magnetic field now reads

$$\hat{H} = i\frac{\gamma a_0}{\ell_B} \times \begin{pmatrix} 0 & -\partial_x - (x - x_c) & 0 & 0 \\ -\partial_x + x - x_c & 0 & 0 & 0 \\ 0 & 0 & 0 & \partial_x - (x - x_c) \\ 0 & 0 & \partial_x + x - x_c & 0 \end{pmatrix}. \tag{19}$$

Of course, this new choice of axes does not affect the eigenvalues of the bulk problem and leaves the effective Hamiltonian $\mathcal{H}_{eff}$ defined in Eq. (7) unchanged but the eigenfunctions have now the following form:

$$\varphi_A = -i\Phi_{n-1} \quad \varphi'_A = i\Phi_n,$$

$$\varphi_B = \Phi_n \quad \varphi'_B = -\Phi_{n-1}, \tag{20}$$

where the $\{\Phi_n\}$ functions are the eigenfunctions of the harmonic oscillator. The phase factor i originates from the orientation of the ribbon. Following the procedure suggested by Brey and Fertig,[21] we now construct an effective Hamiltonian which accounts properly for the armchair boundary conditions. Since, for this type of edge, we have the particular relation $K_y=K'_y$, as argued in Sec. II, the wave functions now read

$$\Psi^{\pm}(\vec{r}) = \begin{pmatrix} \Psi_A^{\pm}(\vec{r}) \\ \Psi_B^{\pm}(\vec{r}) \end{pmatrix}$$

$$= e^{i(K_y+q_y)y}\left[e^{iK_x x}\begin{pmatrix} \varphi_A^{\pm}(x) \\ \varphi_B^{\pm}(x) \end{pmatrix} \pm e^{iK'_x x}\begin{pmatrix} \varphi'^{\pm}_A(x) \\ \varphi'^{\pm}_B(x) \end{pmatrix}\right], \tag{21}$$

where the components $\varphi_{B/A}^{(\prime)\pm}$ must satisfy specific boundary conditions. A crucial difference with zigzag ribbons is that armchair edges are constituted of both A and B sites. As a consequence, *both* components $\Psi_A^{\pm}$ and $\Psi_B^{\pm}$ must vanish on each side of the ribbon: $\Psi^{\pm}(x=0,y)=0$ and $\Psi^{\pm}(x=L,y)=0$. From now on, we choose to explicit these boundary conditions for the left side at $x=0$, what leads to

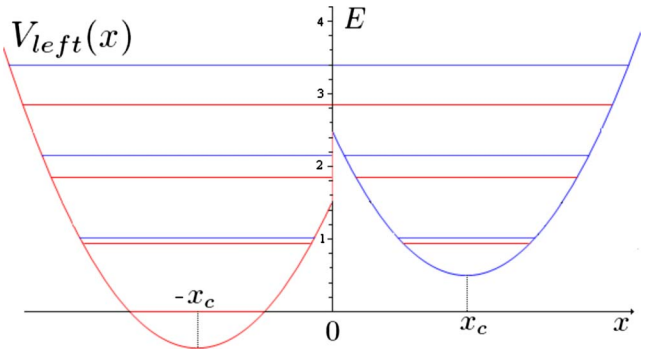

FIG. 11. (Color online) Potential $V_{left}(x)$ for the left edge of an armchair ribbon in a magnetic field. The two wells are centered from a distance $|x_c|$ to the edge $x=0$. The energy levels E_n^+ in blue and E_n^- in red are shown by horizontal lines in each well and have been calculated semiclassically. The energies are dimensionless.

$$\varphi_A^{\pm}(0) = \mp \varphi_A'^{\pm}(0),$$

$$\varphi_B^{\pm}(0) = \mp \varphi_B'^{\pm}(0). \tag{22}$$

Contrary to the zigzag case, the armchair boundary conditions admix the contributions of the two valleys for a given sublattice. In addition, since the Dirac Hamiltonian is first order, the continuity equations [Eq. (22)] on the wave function imply continuity of the derivatives. From Eqs. (19) and (22) we obtain

$$\partial_x \varphi_A^{\pm}|_0 = \pm \partial_x \varphi_A'^{\pm}|_0$$

$$\partial_x \varphi_B^{\pm}|_0 = \pm \partial_x \varphi_B'^{\pm}|_0. \tag{23}$$

Next, as suggested by Brey and Fertig,[21] we build new functions $\Phi^{\pm}$ as

$$\Phi^{\pm}(x) \equiv \varphi_B^{\pm}(-x)\theta(-x) \mp \varphi_B'^{\pm}(x)\theta(x)$$
$$= -i[\varphi_A'^{\pm}(-x)\theta(-x) \mp \varphi_A^{\pm}(x)\theta(x)], \tag{24}$$

where θ is the Heaviside function. Thus, the functions $\Phi^{\pm}$ are solutions of a new effective Schrödinger equation with a potential $V_{left}(x)$ which is $V_u(x)$ for $x>0$ and $V_d(x)$ for $x<0$,

$$\left[-\frac{1}{2}\partial_x^2 + V_{left}(x)\right]\Phi^{\pm}(x) = E_n^{\pm}(x_c)\Phi^{\pm}(x), \tag{25}$$

$$V_{left}(x) = \frac{1}{2}[(|x| - x_c)^2 + \theta(x) - \theta(-x)]. \tag{26}$$

In order to take into account the armchair boundary conditions [Eqs. (22) and (23)], we impose the functions $\Phi_{A/B}^{\pm}$ to satisfy the continuity equations,

$$\Phi^{\pm}(0^+) = \Phi^{\pm}(0^-),$$

$$\partial_x \Phi^{\pm}|_{0^+} = \partial_x \Phi^{\pm}|_{0^-}. \tag{27}$$

The asymmetric potential [Eq. (26)] is shown in Fig. 11. The asymmetry originates from the noncommutativity of x with ∂_x and corresponds to a shift in energy by one Landau level between the two uncoupled wells V_u and V_d. The asymmetric structure of V_{left} is a consequence of the valley admixing imposed by the boundary conditions.

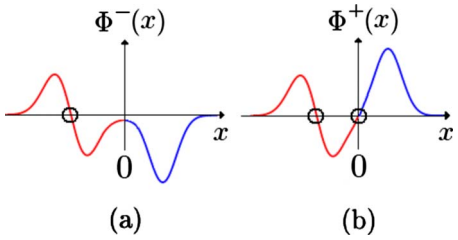

FIG. 12. (Color online) Illustration, for $n=1$, of the two solutions $\Phi^-(x)$ and $\Phi^+(x)$ at the left armchair edge. These solutions do not exhibit the same number of nodes (black circles). (a) The continuity equations generate a wave function Φ^- with $2n-1$ nodes. The functions $\varphi_B^-(-x)$ and $-i\varphi_A'^-(-x)$ are represented on the left (red) whereas $\varphi_B'^-(x)$ and $-i\varphi_A^-(x)$ are represented on the right (blue). (b) The continuity equations generate a wave function Φ^+ with $2n$ nodes. The functions $\varphi_B^+(-x)$ and $-i\varphi_A'^+(-x)$ are represented on the left (red) whereas $\varphi_B'^+(x)$ and $-i\varphi_A^+(x)$ are represented on the right (blue).

We now discuss the qualitative structure of the wave functions. The two combinations $\Psi^{\pm}$ are built with four components $\varphi_{A/B}^{(\prime)\pm}$. When the particle is far from the edge, the system is described by two independent potentials $V_u(x)$ and $V_d(x)$ so that the components $\varphi_{A/B}^{(\prime)\pm}$ take their bulk value given by Eq. (20). Now, close to the edge, the expressions of $\varphi_{A/B}^{(\prime)\pm}$ are modified. In particular, the boundary conditions [Eq. (27)] imply two types of solutions Φ^+ and Φ^-, by matching the components $\varphi_{A/B}^{(\prime)\pm}$ in two different ways. We illustrate this point in Fig. 12 in the case where $n=1$ by showing a qualitative construction of the components $\varphi_{A/B}^{(\prime)\pm}$. The eigenfunction Φ^+ has $2n$ nodes whereas Φ^- has $2n-1$ nodes. As a consequence, the associated eigenvalues $E_n^-(x_c)$ are lower than the eigenenergies $E_n^+(x_c)$, and the valley degeneracy of the energy spectrum is lifted, as seen in Fig. 5. This point is discussed quantitatively in Sec. IV C.

By imposing $\Psi(L,y)=0$, the right edge can now be considered easily in the same way. We obtain a similar effective problem where the potential $V_{left}(x)$ has been replaced by

$$V_{right}(x) = \frac{1}{2}[(|x| + x_c)^2 + \theta(-x) - \theta(x)], \tag{28}$$

where we have performed the translations $x-L \to x$ and $x_c - L \to x_c$ for more commodity in the calculations in the next section. Thus, the potential $V_{right}(x)$ that describes the right edge at $x=L$ is now centered in $x=0$. The potential $V_{right}(x)$ is displayed in Fig. 13.

IV. SEMICLASSICAL TREATMENT

The aim of this section is to calculate analytically the energy spectrum $E_n(x_c)$ for both zigzag and armchair boundary conditions by using a semiclassical formalism. The eigenenergies are solutions of effective Schrödinger equations in appropriate potentials: a double symmetric harmonic potential $V_A(x)$ (Fig. 10) for the zigzag case and a double

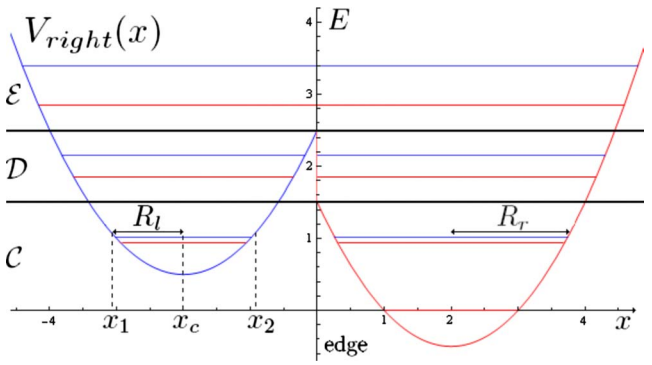

FIG. 13. (Color online) Potential $V_{right}(x)$ of the right armchair edge in a magnetic field with the dimensionless energies E_n calculated semiclassically. Here $x_c=-2$. The three regions $\mathcal{C}$, $\mathcal{D}$, and $\mathcal{E}$, such as the cyclotron radii R_l and R_r refer to the Sec. IV.

asymmetric harmonic potential $V_{right}(x)$ (Fig. 13) for the armchair case. We develop here two approaches. In the first one (Sec. IV A), we assume that the two wells of the potentials are uncoupled, and quantize the action with the Bohr-Sommerfeld rule. The second approach (Sec. IV B), based on the WKB formalism, properly accounts for the overlap of the wave function between the two wells. From now on, we only focus on the right edge of the ribbons, and take $\hbar=1$.

A. Semiclassical quantization of the action

We first define the classical cyclotron radius R. For the zigzag case, R is given by $E=1/2(R^2+1)$ as illustrated in Fig. 10. For the armchair case, since the potential $V_{right}(x)$ is asymmetric, we need to define two classical cyclotron radii R_l and R_r (see Fig. 13). Next, we introduce an action S associated with these potentials. Along a closed path, the action is given by

$$S(E,x_c)=2\int_{x_1}^{x_2} dx\sqrt{2[E-V(x)]}, \tag{29}$$

where x_1 and x_2 are the positions of the turning points, and $V(x)$ is either $V_A(x)$ or $V_{right}(x)$. Such an action is quantized with the Bohr-Sommerfeld rule as

$$S(E,x_c)=2\pi[n+\gamma(E,x_c)], \tag{30}$$

where $n\geq 0$ is an integer and $0<\gamma(E,x_c)<1$ is a function that encodes all the information on the connection procedure at the turning points. For a harmonic potential, $\gamma=1/2$. Here, for the double well potentials, $\gamma(x_c,E)$ is not a constant anymore but depends on the energy and on the distance to the edge because of the overlap of the wave function between the two wells. We assume in this section that the two wells are uncoupled so that we take γ as a constant.

Now we have to specify distinct regions in energy, each of them requiring an appropriate semiclassical treatment. These regions are delimited by horizontal thick lines in Figs. 10 and 13 and involve different expressions of the action $S(E,x_c)$ given by Eq. (29).

1. Zigzag ribbons

We consider the potential $V_A(x)$ that describes the right zigzag edge for the $\vec{K}$ valley (Fig. 10). We recall that the right edge is located at $x=0$. For a given energy E, we have to discuss two distinct regions: $|x_c|>R$ (region $\mathcal{A}$) and $|x_c|<R$ (region $\mathcal{B}$), where $R=\sqrt{2E-1}$ is the cyclotron radius.

(1) *Region* $\mathcal{A}$: $|x_c|>R$. The turning points are defined by $x_1=x_c-R$ and $x_2=x_c+R$ so that the action [Eq. (29)] in the left well is simply,

$$S_{\mathcal{A}}(R)=\pi R^2. \tag{31}$$

A simple calculation of the energies by quantizing $S_{\mathcal{A}}$ with the constant value $\gamma=1/2$ in Eq. (30) leads to the Landau levels $E_n=n+1$ with $n\geq 0$, and therefore to the spectrum $\epsilon_n\propto\sqrt{B(n+1)}$ in this region. The $n+1$ term originates from the energy shift of the potential $V_A(x)$. The rest of the spectrum near the right edge is given by the contribution of the other valley. Therefore, by treating the same way the potential $V'_A(x)$, we find the spectrum $E_n=n$ with $n\geq 0$. Finally, we obtain a set of degenerated energies $E_n=n$ with $n\geq 1$, and a nondegenerated level $E_0=0$ what gives the expected valley degenerated graphene energy levels $\epsilon_n\propto\pm\sqrt{Bn}$ for $n\geq 0$.

(2) *Region* $\mathcal{B}$: $|x_c|<R$. The left turning point x_1 is unchanged but the right turning point is replaced by $x_2=0$ so that the action reads

$$S_{\mathcal{B}}(R,x_c)=R^2\left[\theta-\frac{1}{2}\sin(2\theta)\right], \tag{32}$$

where we have introduced the parameter $\theta\equiv\arccos\frac{x_c}{R}$. The spectrum depends now on the distance x_c to the edge. The total action in the double well $S_t=2S_{\mathcal{B}}$ is quantized as $S_t=2\pi(p+1/2)$. We recall that we have to keep only the antisymmetric solutions which have an odd number of nodes, what implies $p=2n+1$. Therefore, such a quantization leads to

$$S_{\mathcal{B}}(R,x_c)=2\pi\left(n+\frac{3}{4}\right). \tag{33}$$

We recover the result $\gamma=3/4$ for a harmonic potential cut by an infinite barrier potential.[31] By identifying the two expressions (32) and (33), we finally obtain a set of self-consistent equations labeled by the integer n for $E_n(x_c)$, from which we can extract the energy spectrum.

The spectrum $E_n(x_c)$ obtained within this approach for the right zigzag edge in the $\vec{K}$ valley is plotted in Fig. 15. In order to correctly describe the region where $|x_c|\approx R$, we use in Sec. IV B a more sophisticated approach based on the WKB formalism.

2. Armchair ribbons

Because of the asymmetry of the potential $V_{right}(x)$, we have now to distinguish three regions ($\mathcal{C}$, $\mathcal{D}$, and $\mathcal{E}$ in Fig. 13). In each one, we consider two actions, S_l for the left well and S_r for the right well. In addition, the levels in the left or in the right well will be indexed by different integers n_l, $n_r\geq 0$. The energy is given by $E=(R_l^2+1)/2=(R_r^2-1)/2$,

where R_l (respectively, R_r) is the cyclotron radius for the left (respectively, right) well (note that $R_r^2-R_l^2=2$).

(3) *Region* $\mathcal{C}$: $R_l \leq R_r \leq |x_c|$. In each well, the action still has the form given by Eq. (31) so that we write

$$\text{left well:} S_l = S_{\mathcal{A}}(R_l),$$

$$\text{right well:} S_r = S_{\mathcal{A}}(R_r). \tag{34}$$

By using the Bohr-Sommerfeld rule [Eq. (30)] with $\gamma=1/2$ for both S_l and S_r, we find the energies $E_{n_l}=n_l+1$ into the left well and $E_{n_r}=n_r$ into the right well, and then $n \equiv n_r=n_l+1$. This leads to the degenerated Landau levels $E_n=n$ with $n \geq 1$ and a nondegenerated level $E_0=0$.

(4) *Region* $\mathcal{D}$: $R_l \leq |x_c| \leq R_r$. Now, because of the step in the potential, the action S_r has the form given by Eq. (32), whereas S_l is unchanged. The two actions read

$$\text{left well:} S_l = S_{\mathcal{A}}(R_l),$$

$$\text{right well:} S_r = S_{\mathcal{B}}(R_r, x_c). \tag{35}$$

The action S_l is still quantized as previously, what simply gives the spectrum $E_n=n$ with $n \geq 1$. As the wave function inside the right well does not totally vanish in $x=0$, the situation is different than in the case of an infinite potential barrier. This suggests a choice closer to $\gamma=1/2$ rather than $\gamma=3/4$ for the quantization of the action S_r. By doing so, we obtain an implicit equation in E_n and x_c from which we can extract the spectrum $E_n(x_c)$. Of course, we understand that the region $\mathcal{D}$ is necessarily badly described by such an approach and specifically requires a more sophisticated method since γ cannot be a constant anymore.

(5) *Region* $\mathcal{E}$: $|x_c| \leq R_l \leq R_r$. In this region, we need to consider the total action that reads

$$S_{\mathcal{E}} = S_{\mathcal{B}}(R_l, x_c) + S_{\mathcal{B}}(R_r, x_c), \tag{36}$$

where the function S_B is given in Eq. (32). This expression is still valid when x_c crosses the edge. Since the two turning points both touch a harmonic potential, this action is simply quantized by the usual Bohr-Sommerfeld rule with $\gamma=1/2$ what also leads to an implicit equation in $E_{n'}$ and x_c, where n' is a different integer than n since there are twice more solutions in this region than in the regions $\mathcal{A}$ or $\mathcal{C}$.

The armchair spectrum obtained within this approach is shown in Fig. 17. It perfectly matches with numerical solutions of the Schrödinger equation [Eq. (25)] except around the intermediate region $\mathcal{D}$. In the following, we describe quantitatively all the regions by keeping $\gamma=\gamma(E,x_c)$ and calculating the spectra of zigzag and armchair ribbons by accounting for the coupling between the two wells. We give now the general picture of the method which is detailed in the Appendix A.

B. WKB approach

In this section, we present a method based on the WKB formalism to account for the overlap of the wave function between the two wells. This approach is detailed in the Appendix A. Technically, it brings us to calculate the function $\gamma(E,x_c)$. For this purpose, we express the wave function inside the left well within the WKB approximation as

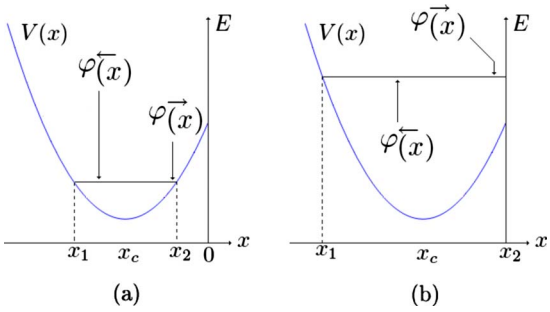

FIG. 14. (Color online) Illustration of the two typical different situations we have to distinguish for the semiclassical calculation. (a) The two turning points x_1 and x_2 are on the parabola. (b) The turning point $x_2=0$ is not on the parabola. These two situations involve different expressions of the action $S(E,x_c)=S_l$ in the left well. Same considerations have to be made for the right well.

$$\varphi^{\leftarrow}(x) = \frac{C}{\sqrt{k(x)}} \sin\left[\mathcal{S}(x_1,x) + \frac{\pi}{4}\right] \tag{37}$$

with C a constant and where

$$\mathcal{S}(x_1,x) = \int_{x_1}^{x} dx' \sqrt{E - V(x')} \tag{38}$$

is the partial action between the turning point x_1 and an arbitrary position x inside the left well. Close to the right turning point x_2, this approximation breaks down. In order to find a valid approximation of the wave function in this region, we linearize the harmonic potential so that the eigenfunctions of the Schrödinger equation are a combination of Airy functions, that is,

$$\varphi^{\rightarrow}(x) = \alpha_l \,\mathrm{Ai}[f_l(x,E,x_c)] + \beta_l \,\mathrm{Bi}[f_l(x,E,x_c)], \tag{39}$$

where α_l and β_l are constants and $f_l(x,E,x_c)$ is a function that depends on the region $\mathcal{A}$, $\mathcal{B}$, $\mathcal{C}$, $\mathcal{D}$, or $\mathcal{E}$ so that each region must be treated separately. By imposing the equality between $\varphi^{\leftarrow}(x)$ and the asymptotic expansion of $\varphi^{\rightarrow}(x)$ inside the well, we obtain a relation between the constants and the action S_l which is given by the relation [Eq. (29)]. We need to distinguish the cases $x_2 \neq 0$ and $x_2=0$ (Fig. 14), for which the matching condition gives

$$x_2 \neq 0: \quad \tan S_l/2 = \alpha_l/\beta_l,$$

$$x_2 = 0: \quad \tan(S_l/2 + \delta_l) = \alpha_l/\beta_l, \tag{40}$$

where $\delta_l=\delta_l(E,x_c)$ is a known function originating from the step between the energy E at the turning point $x_2=0$ and the potential $V(0)$. The same procedure must be performed for the right well where we obtain similar relations between the ratio α_r/β_r and the action S_r calculated between the two turning points in the right well,

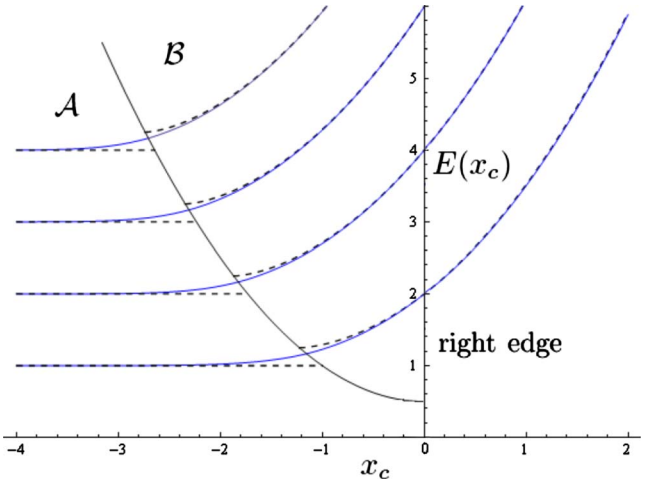

FIG. 15. (Color online) Dimensionless eigenenergies $E_n(x_c)$ of the double symmetric harmonic oscillator potential $V_A(x)$ calculated analytically (continuous line) within the WKB method and (dashed line) within the Bohr-Sommerfeld quantization rule with $\gamma=\frac{1}{2}$ in region $\mathcal{A}$ and $\gamma=\frac{3}{4}$ in region $\mathcal{B}$. The solutions we keep correspond to the antisymmetric solutions of the double symmetric well.

$$x_3 \neq 0: \quad \tan S_r/2 = \alpha_r/\beta_r,$$

$$x_3 = 0: \quad \tan(S_r/2 + \delta_r) = \alpha_r/\beta_r, \tag{41}$$

where x_3 is the left turning point in the right well.

To determine the ratio α_l/β_l, we impose the continuity of the wave function and its derivative between the two wells. By doing so, we obtain one equation with the two unknown quantities α_l/β_l and α_r/β_r. Next, by injecting $S_r=S_t-S_l$ into Eq. (41), where the total action S_t is calculated explicitly as a function of E and x_c, we obtain a second-order polynomial in α_l/β_l what yields two solutions. Because of the relation [Eq. (40)], the action is quantized as $S_l=2\pi(n+\gamma_l)$ which is the Bohr-Sommerfeld quantization. Thus, the two solutions of the polynomial yield the two solutions $\gamma_l^{\pm}(E,x_c)$.

Next, by using formula (29), we calculate explicitly the expression of the action S_l as a function of E and x_c, which we identify with the action given by the Bohr-Sommerfeld rule previously found. As we know the functions $\gamma_l^{\pm}(E,x_c)$, we finally obtain two analytical self-consistent equations in E and x_c for a given n, one with γ_l^+ and the other one with γ_l^-. The spectrum $E_n(x_c)$ can then be extracted for a given n. The whole procedure must be performed for each region $\mathcal{A}$ to $\mathcal{E}$ where the action has different expressions as discussed in the previous section. All this study is detailed in the Appendix A for both the symmetric and the asymmetric potentials.

C. Quantitative analytical results

We give here the spectra obtained for the effective potentials $V_A(x)$ [zigzag case, Eq. (18)] and $V_{right}(x)$ [armchair case, Eq. (28)], within the two semiclassical approaches introduced above.

1. Symmetric potential (zigzag)

The energy levels $E_n(x_c)$ of the double symmetric harmonic potential $V_A(x)$ describing the contribution of the $\vec{K}$ valley at the right zigzag edge (see Fig. 10) are shown in Fig. 15. The two regions $|x_c|>R$ and $|x_c|<R$ are separated by a parabola of equation $E=(x_c^2+1)/2$. In the spectrum of Fig. 15, we have only kept the higher energy solution of the double well problem since they correspond to the eigenenergies of the antisymmetric eigenfunctions. The dashed lines correspond to the approximation where $\gamma=cst$, what leads to an unphysical discontinuity around $|x_c|=R$. The continuous lines represent the energy levels obtained within the WKB approximation. The solutions found with this method in regions $\mathcal{A}$ and $\mathcal{B}$ perfectly match at $|x_c|=R$. Next, we show in Fig. 16 the structure of the edge states spectrum in the $\vec{K}$ valley for both the left and right edges. The right (blue) part of the spectrum, is the energy spectrum on the right edge calculated within the WKB method and already displayed in Fig. 16, whereas the left (red) part represents the edge states on the left side of the ribbon in the same $\vec{K}$ valley. The effective problem for the left edge is obtained in a similar way than for the right edge (see Sec. III B) where we have considered the potential $V_d(x)$ and the boundary condition $\varphi_B(x=0)=0$. Note that we recover the particular relation $\epsilon_n^{edge}=\epsilon_{2n+1}^{bulk}$ with $n\geq 0$ on the left edge and $\epsilon_n^{edge}=\epsilon_{2n}^{bulk}$ with $n>0$ for the right edge. This peculiar property of the edge states is due to the fact that we have to keep only the antisymmetric eigenfunctions of the double well problem. In particular, when $x_c=0$, the double well is simply a single harmonic well, so as the bulk potentials. In addition, the shift of this distribution between the two edges is due to the shift in energy between the potentials $V_A(x)$ and $V_B(x)$ that, respectively, originate from the potentials $V_u(x)$ and $V_d(x)$ modified by the zigzag boundary conditions. We have emphasized this point by dashed lines in Fig. 16. This explains the remarkable structure of the zigzag edge states discussed in Sec. II B. Finally, the mirror symmetry between the valleys $\vec{K}$ and $\vec{K}'$ emphasized in Fig. 6 is now clear, since the edge potentials into the $\vec{K}'$ valley, that are $V_A'(x)$ for the right edge and $V_B'(x)$ for the left edge, now originate from the bulk potentials $V_d(x)$ and $V_u(x)$, respectively, with the zigzag boundary conditions.

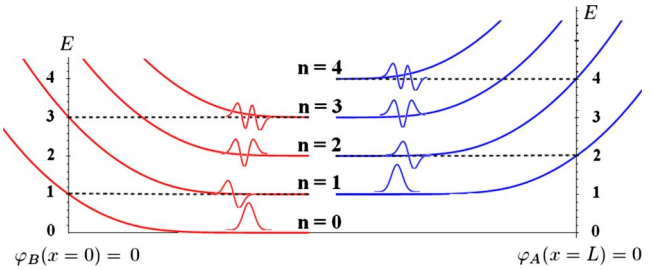

FIG. 16. (Color online) Dimensionless zigzag edge states $E_n(x_c)$ of the $\mathcal{H}_{eff}$ problem in the $\vec{K}$ valley. We have represented the bulk wave function of each sublattice [left (red) for B sublattice and right (blue) for A sublattice]. The results have been obtained within the WKB approximation.

2. Asymmetric potential (armchair)

For the armchair case, we have to keep all the solutions of the double asymmetric potentials $V_{left}(x)$ and $V_{right}(x)$. As

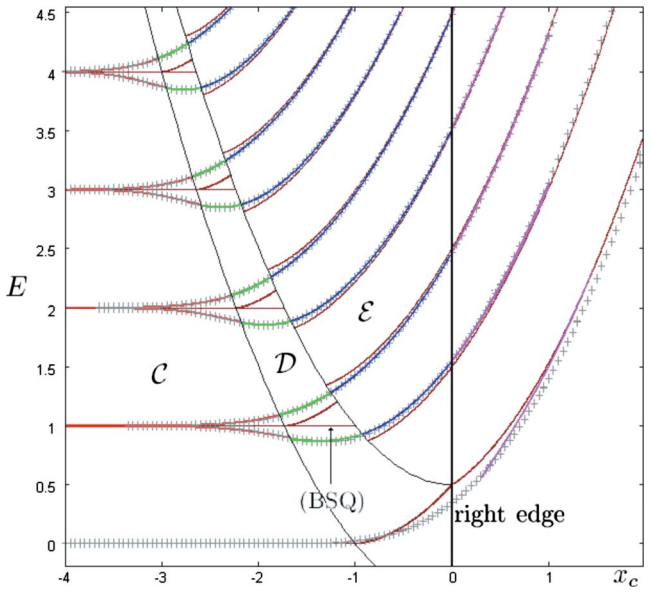

FIG. 17. (Color online) Dimensionless energies $E_n(x_c)$ of the armchair edge states. The results obtained with three different methods are shown. The discontinuous brown lines are the levels obtained by taking $\gamma=cst$ in the Bohr-Sommerfeld quantization (BSQ). The colored continuous lines have been obtained within the WKB approach. The different colors in regions $\mathcal{C}$, $\mathcal{D}$, and $\mathcal{E}$ are associated to the different semiclassical behaviors of the particle in Fig. 19, as discussed in the next section. The gray crosses represent the numerical solutions for the energy levels in the potential $V_{asym}(x)$. We show that the results obtained within the WKB approximation perfectly fit the numerical calculations, except for $n=0$.

discussed in Sec. III C and illustrated in Fig. 12, the wave functions of the effective Schrödinger equation with armchair boundary conditions [Eq. (25)] have, for a given n, either $2n$ nodes or $2n-1$ nodes, what leads to pairs of eigenenergies $E_n^{\pm}(x_c)$. The semiclassical energies $E_n(x_c)$ are displayed in Fig. 17. The three regions $\mathcal{C}$, $\mathcal{D}$, and $\mathcal{E}$ are separated by the parabola parametrized by $|x_c|=R_l$ and $|x_c|=R_r$ that are $E=\frac{1}{2}(x_c^2+1)$ and $E=\frac{1}{2}(x_c^2-1)$. Contrary to the simple semiclassical calculation with $\gamma=cst$ (discontinued brown lines), the WKB method gives a perfect matching between the three regions and is in very good agreement with numerical calculations (gray crosses). The nonmonotonous dependence of the energy levels $E_n^-(x_c)$ appears as the result of the competition between two effects. When x_c approaches the edge, the two potential wells of the effective model become more and more coupled so that the twofold degeneracy is lifted and the lowest level decreases when x_c increases. When x_c further increases, the confinement becomes so strong that $E_n^-(x_c)$ has to increase.

D. Drift velocity

We now briefly comment on the behavior of the drift velocity v_d along the edges. It is given by the derivative $v_d=\partial\epsilon/\partial k_y=\ell_B\partial\epsilon/\partial x_c$. Interestingly, in the armchair case, the nonmonotonous behavior of the edge state energies when approaching the edge implies a change in sign of the drift velocity in a finite range of x_c. From the discussion of the above Sec. IV C 2, this negative drift velocity is due to the lift of the valley degeneracy when x_c approaches the edge. We also point out that the (positive) drift velocity saturates toward the Fermi velocity when x_c increases further. This is easily understood from the following semiclassical argument. When x_c is largely outside the ribbon, the cyclotron radius is necessarily of order x_c. Therefore the energy E, solution of the effective Hamiltonian $\mathcal{H}_{eff}$ [Eqs. (8) and (9)], is of order $E=R^2/2\to x_c^2/2$. Using Eq. (12), we obtain $v_d=\ell_B\partial\epsilon/\partial x_c=v_F\partial\sqrt{2E}/\partial x_c\to v_F$.

V. QUANTIZED SKIPPING ORBITS

In this section, we propose a simple interpretation of the results in terms of a semiclassical picture for skipping orbits. Consider the action S associated with the effective Schrödinger equations with the potentials obtained for the zigzag case. These four equations (one per edge and per valley) describe the motion of a free massive particle in a magnetic field (all units being set to one) in the presence of an infinite potential barrier or the image of the harmonic potential, as illustrated in Figs. 9 and 10 for the right edge in the $\vec{K}$ valley. From the classical equations of motion, the action $S=\oint\vec{p}\cdot d\vec{r}$ along a closed trajectory for a given energy is simply related to the area $\mathcal{A}$ enclosed by the corresponding periodic orbit,

$$\mathcal{S}(E,x_c)=\oint\vec{p}\cdot d\vec{r}=\frac{eB}{2}\oint\vec{r}\times d\vec{r}=eB\mathcal{A} \tag{42}$$

so that the Bohr-Sommerfeld quantization rule [Eq. (30)] implies the quantization of the area

$$\mathcal{A}(E,x_c)=2\pi(n+\gamma)\ell_B^2 \tag{43}$$

in our units where $\hbar=1$. In the bulk of the system, that is, when the distance $|x_c|$ to the edge is larger than the cyclotron radius R, we have simply

$$\mathcal{A}(E)=\mathcal{S}(E)=2\pi(n+\gamma) \tag{44}$$

and the distances are measured in units of ℓ_B. This quantization implies the quantization of the cyclotron radius R. Taking $\gamma=1/2$, $\mathcal{A}=\pi R^2=2\pi(n+1/2)$ so that $R_n^2=2n+1$, we deduce the energy levels, $E_n=R_n^2/2\pm1/2=n$, and obtain the bulk spectrum of Landau levels $E_n=n$.

When $|x_c|$ becomes smaller than R, the classical orbits skip along the wall represented by the infinite potential well, and they form open orbits. As already noticed,[32,33] the area to be quantized is the area delimited by the skipping orbit and the wall. In this case, the action calculated in Eq. (32) has a very simple interpretation in terms of skipping orbits since the parameter $\theta=\arccos\frac{x_c}{R}$ has a clear geometrical meaning shown in Fig. 18. The action is nothing but the area enclosed by the skipping orbit,

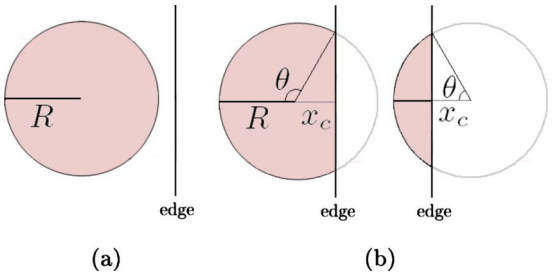

FIG. 18. (Color online) Classical cyclotron orbits for the "effective" particle associated to the effective Hamiltonian $\mathcal{H}_{eff}$ close to a zigzag edge. (a) The closed cyclotron orbit encloses an area $\mathcal{A}$ quantized by the Bohr-Sommerfeld rule [Eq. (47)], and the resulting Landau levels spectrum is displayed in Fig. 15 (region $\mathcal{A}$). (b) The particle is skipping along the edge and the edge states energy spectrum (region $\mathcal{B}$ in Fig. 15) is obtained from the quantization rules [Eq. (47)].

$$\mathcal{A}(E,x_c) = R^2\left[\theta - \frac{1}{2}\sin(2\theta)\right]. \tag{45}$$

We can now interpret semiclassically the energy spectra obtained in the above sections.

For the zigzag edge, the two regions $\mathcal{A}$ and $\mathcal{B}$ in the spectrum (Fig. 15) can be associated to the two distinct cases represented in Fig. 18,

$$\text{(a) region } \mathcal{A}, \quad \mathcal{A}(E) = \pi R^2 = 2\pi\left(n + \frac{1}{2}\right),$$

$$\text{(b) region } \mathcal{B}, \quad \mathcal{A}(E,x_c) = \frac{R^2}{2}(2\theta - \sin 2\theta) = 2\pi\left(n + \frac{3}{4}\right) \tag{46}$$

from, which together with the relation $E=R^2/2\pm 1/2$, we have deduced the energy levels, except near the region $x_c \simeq -R$.

For the armchair case, the situation is more involved since we describe the classical motion of a massive particle *in the presence of its shifted image* (Fig. 19). Since the potential is asymmetric, we have defined two cyclotron radii related to the energy E as $E=R_l^2/2+1/2=R_r^2/2-1/2$. Now we have to consider three different cases corresponding to the regions $\mathcal{C}$, $\mathcal{D}$, and $\mathcal{E}$ in Fig. 17.

In the region $\mathcal{C}$ where $|x_c|>R_r>R_l$, the orbit and its image are both closed cyclotron orbits. The quantization of their area,

$$\text{left side:} \quad \mathcal{A}_l = \pi R_l^2 = 2\pi\left(n_l + \frac{1}{2}\right),$$

$$\text{right side:} \quad \mathcal{A}_r = \pi R_r^2 = 2\pi\left(n_r + \frac{1}{2}\right) \tag{47}$$

leads to the the energy levels given by $E_n=n$, with $n=n_r=n_l+1$, what quantize the cyclotron radii as $R_r=\sqrt{2n+1}$ and $R_r=\sqrt{2n-1}$, the latest does not allow the $n=0$ level.

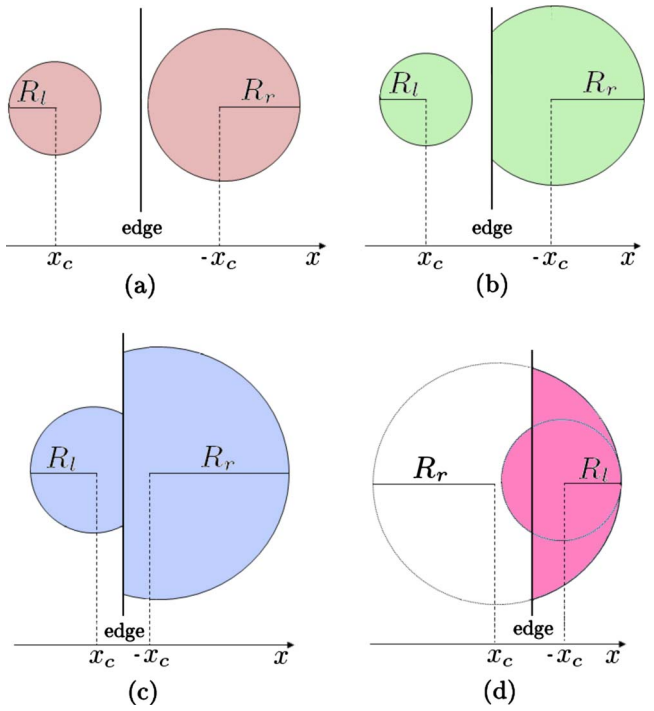

FIG. 19. (Color online) Classical cyclotron orbits for the effective particle associated to the effective Hamiltonian, close to an armchair edge. (a) Each cyclotron orbit encloses an area $\mathcal{A}_l$ or $\mathcal{A}_r$, each of them quantized by the Bohr-Sommerfeld rule [Eq. (30)]. For an energy level $E_n=n$, one has $R_l=\sqrt{2n-1}$ and $R_r=\sqrt{2n+1}$. The ground state $n=0$ has no component on the left side. The associated spectrum is the bulk Landau levels spectrum displayed in the region $\mathcal{C}$ in Fig. 17(b) When the left orbit approaches the edge, its image becomes a skipping orbit. This lifts the degeneracy between the energy levels as seen in Fig. 17 (region $\mathcal{D}$). [(c) and (d)] When x_c is closer to the edge, both orbits are open skipping orbits. The quantization of the total area leads to the spectrum in region $\mathcal{E}$ of Fig. 17.

In the region $\mathcal{D}$ where $R_r>|x_c|>R_l$, the left orbit is still closed but its image is a skipping orbit. Keeping the notation $n=n_r=n_l+1$, we have, defining $\theta_r=\arccos\frac{x_c}{R_r}$,

$$\text{left side:} \mathcal{A}_l = \pi R_l^2 = 2\pi\left(n - \frac{1}{2}\right) \quad n>0,$$

$$\text{right side:} \mathcal{A}_r = R_r^2\left(\theta_r - \frac{1}{2}\sin 2\theta_r\right) = 2\pi\left(n + \frac{1}{2}\right) \quad n \geq 0 \tag{48}$$

from which we obtain the energy levels in region $\mathcal{D}$. The degeneracy lift is classically explained by the fact that both orbits have a different structure. The left orbit is closed and its semiclassical energy is still $E_n=n+1$ while the energy associated with the right skipping trajectory increases with x_c. Note that it is in this peculiar region that an inversion of the slope occurs.

In the region $\mathcal{E}$ where $R_r>R_l>|x_c|$, both orbits are open and the area to be quantized is the total area

$$\mathcal{A}_l + \mathcal{A}_r = 2\pi\left(n' + \frac{1}{2}\right) \quad n' \geq 0, \tag{49}$$

$$\mathcal{A}_l = R_l^2\left(\theta_l - \frac{1}{2}\sin 2\theta_l\right),$$

$$\mathcal{A}_r = R_r^2\left(\theta_r - \frac{1}{2}\sin 2\theta_r\right), \tag{50}$$

where θ_l and θ_r are defined such that $x_c = R_l \cos\theta_l = R_r \cos\theta_r$. Since the action has almost doubled from region $\mathcal{D}$ to region $\mathcal{E}$, the resulting energy spectrum is twice denser, and the twofold degeneracy of the levels has been removed.

VI. TWO EDGES

Up to now, we have considered the evolution of the spectrum in the vicinity of one edge. If the two edges are sufficiently far apart compared to the cyclotron length ℓ_B, the spectrum can be treated independently on both sides. We now consider the case of a narrow ribbon, whose width L is on the order of a few magnetic lengths. The low-energy spectrum in a ribbon of width $L=9.6\ell_B$ is shown in Figs. 20(a) and 21(b), respectively, for zigzag and armchair ribbons.

In the zigzag case, in each valley, the spectrum clearly exhibits three different regions, which correspond to the geometry of the orbits depicted in Fig. 20(b). Regions $\mathcal{A}$ corresponds to bulk cyclotron orbits. Regions $\mathcal{B}_l$ and $\mathcal{B}_r$ have been already discussed and correspond to a skipping orbit along a single boundary (left or right). Each sublattice is characterized by a cyclotron orbit (in K valley, small blue orbit for A sites and large pink orbit for B sites; the opposite for the K' valley). As explained in the text, in K valley, the A cyclotron orbits sees only the right edge and the B cyclotron orbits sees only the left edge (the opposite in the K' valley). At high energy, the new region $\mathcal{J}$ corresponds to the situation where both cyclotron orbits intersect the two boundaries. The black curves correspond to the situations where a cyclotron orbit precisely touches a boundary. Their equation is

$$\epsilon(k_y) = t\frac{\sqrt{3}a_0}{2}\sqrt{(q_y - \Delta q_y)^2 \pm 1/\ell_B^2}, \tag{51}$$

where $\Delta q_y = 0$ for the left edge and $\Delta q_y = L/\ell_B^2$ for the right edge. By a simple quantization of the areas shown in Fig. 20(b), one can obtain the full low-energy spectrum in a very good approximation, excepted when the orbits graze the boundaries, that is in the vicinity of the black curves. It is obvious on this figure that the two edges do not play exactly the same role, and that, for a given valley, the spectrum is not exactly symmetric. Furthermore, in each valley, an additional asymmetry is seen at high energy because the linear approximation of the low-energy Hamiltonian breaks [Eq. (7)] down.

The case of armchair boundary conditions is more involved. In Fig. 21(a), one can distinguish nine regions, which corresponds to the geometries of the classical orbits depicted in Fig. 21(b). The black curves correspond to the situations where a cyclotron orbit precisely touches a boundary. Their equation is given by Eq. (51). Region $\mathcal{C}$ corresponds to bulk cyclotron orbits. The blue cyclotron orbits are related to the A and B' eigenfunctions, whereas the pink cyclotron orbits are related to the A' and B eigenfunctions. Regions $\mathcal{E}_l$ and $\mathcal{E}_r$ have been already discussed and correspond to skipping orbits along a single boundary (left or right). In the intermediate regions $\mathcal{D}_l$ and $\mathcal{D}_r$, only one of the two orbits touches the edge. At high energy, in the region $\mathcal{I}$, the two cyclotron orbits touch the two edges of the ribbon. The more exotic regions $\mathcal{F}$, $\mathcal{G}_l$, and $\mathcal{G}_r$ have a simple geometric interpretation in Fig. 21(b).

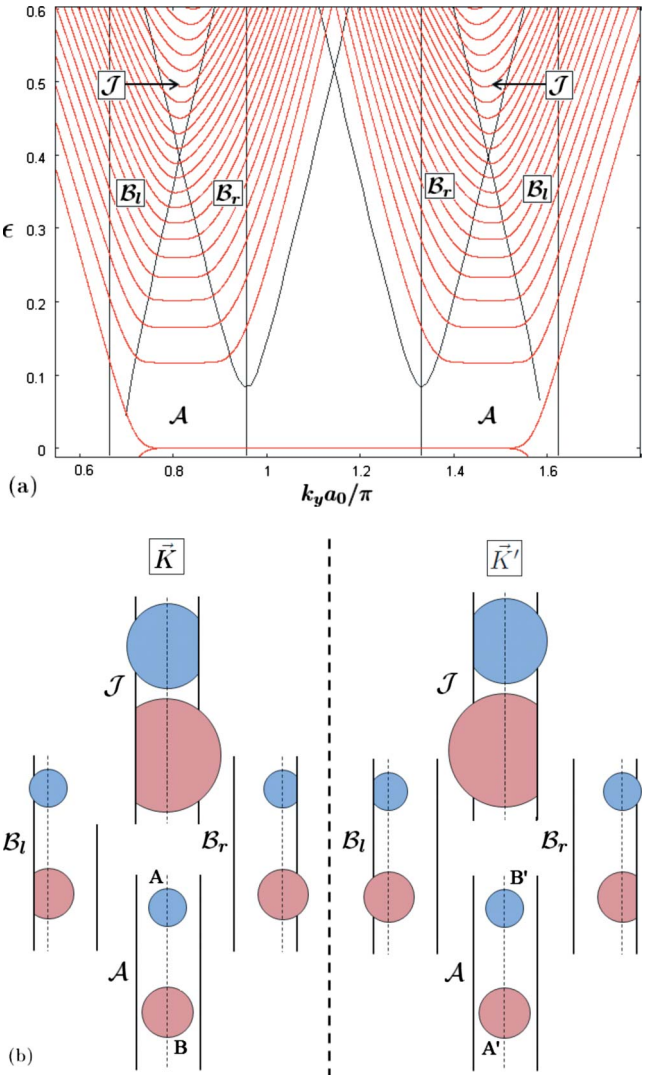

FIG. 20. (Color online) (a) Red curves: low-energy spectrum for a zigzag ribbon in a magnetic field in units of t. The width L of the ribbon is $L=174a$ and the dimensionless magnetic flux f is $f=0.00126$ so that $L/\ell_B=9.6$. The black curves indicate the situations where the classical cyclotron orbits touch an edge. (b) Schematic representation of the different situations for the position of the cyclotron orbits with respect to the edges of the ribbon, as discussed in the text.

VII. CONCLUSION

We have investigated the spectra of graphene ribbons in a magnetic field with zigzag and armchair boundary condi-

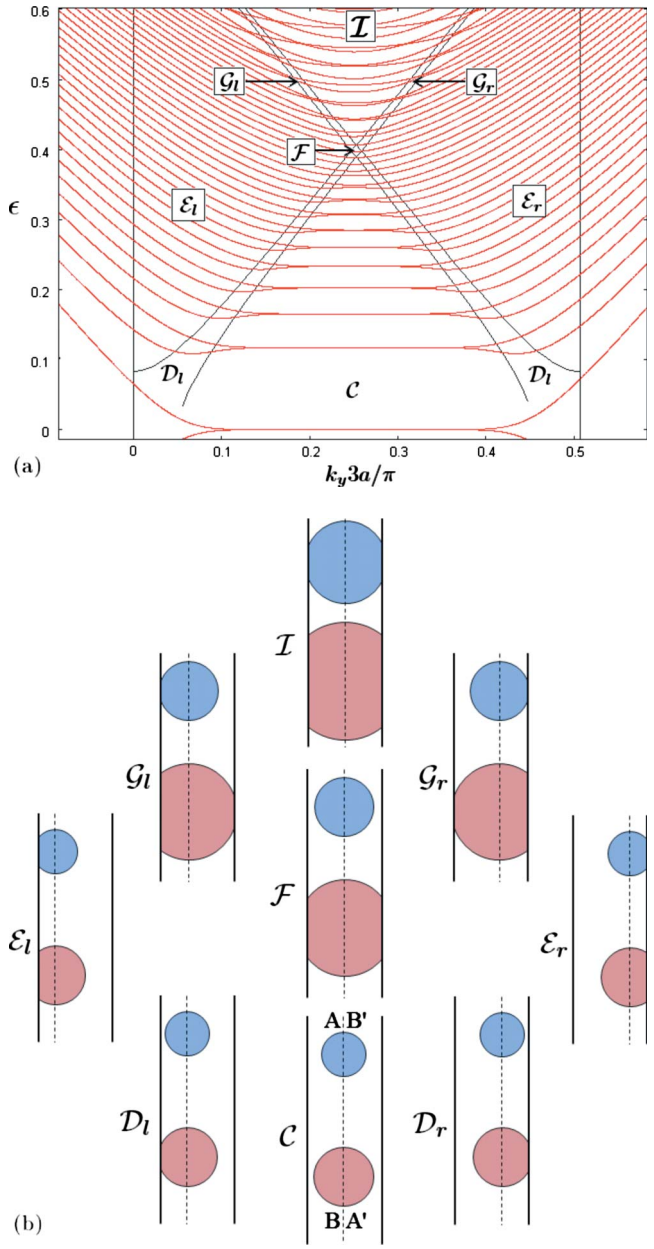

FIG. 21. (Color online) (a) Red curves: low-energy spectrum for an armchair ribbon in a magnetic field in units of t. The width L of the ribbon is $L=201a_0/2$ and the dimensionless magnetic flux f is $f=0.00126$ so that $L/\ell_B=9.6$. The black curves indicate the situations where the classical cyclotron orbits touch an edge. (b) Schematic representation of the different situations for the position of the cyclotron orbits with respect to the edges of the ribbon.

tions. We have first revisited these spectra numerically and revealed a remarkable structure in the repartition of the edge states in zigzag ribbons that we explain in this paper. We notice that these remarkable behaviors of the edge states could be observed by scanning tunneling microscopy or spectroscopy techniques.[23,34–36]

Next we have described and calculated these edge states with simple analytic tools. For both types of ribbons, effective Schrödinger equations with a specific double well potential have been derived at low energy. This potential is asymmetric in energy when the valleys $\vec{K}$ and $\vec{K}'$ are coupled (armchair edge) and symmetric otherwise (zigzag edge). The eigenenergies of these potentials have been calculated numerically recently.[23] Another recent work[37] provided a semiclassical framework to study analytically the edge states for both zigzag and armchair edges but this approach does not furnish the full low-energy spectrum. We have developed here two semiclassical methods to calculate the energy edge states analytically. A very simple one consists in using the Bohr-Sommerfeld quantization of the action related to the effective Schrödinger equations. This approximation captures the essential of the physical picture except when the cyclotron radius of the effective particle is on the order of the distance to the edge. This approach also reveals different regions as a function of the energy and the distance to the edge, where the skipping orbits are quantized in different ways. The second method is based on the WKB formalism, and accounts for the overlap of the wave function when it is close to the edge. Consequently, this more sophisticated analytical approach perfectly describes the edge states whatever the distance of the center of the cyclotron motion to the edge. In particular, it quantitatively describes an interesting region in the armchair case (called region $\mathcal{D}$ in the paper) where the energy does not increase monotonously. This implies that the drift velocity along the edge may change in sign when the position x_c varies. These WKB results perfectly fit numerical exact calculations. We have considered only two special types of boundaries and one may wonder what is the nature of the edge states for any orientation of the edges. This question has already been addressed concerning the existence of edge states in zero field, see, for example.[13] This careful study has shown that the generic situation corresponds to the zigzag case. It would be interesting to confirm this statement in the presence of a magnetic field. For this purpose, it is useful to stress that for any orientation of the edges, we always have K_y different from K'_y, as seen in Fig. 2 (y being the direction of the ribbon), except for the armchair geometry. Therefore we expect the armchair case to be special in the sense that the valleys are coupled (since $K_y=K'_y$) and the other situations to correspond to uncoupled valleys like in the zigzag case. A more precise systematic study is certainly of great interest but beyond the scope of the present work.

ACKNOWLEDGMENTS

We acknowledge useful discussions with J.-N. Fuchs and M.-O. Goerbig. This work is supported by the NANOSIM-GRAPHENE Project (Project No. ANR-09-NANO-016-01) of ANR/P3N2009.

APPENDIX A: THE WKB METHOD

In the whole appendix, we define the classical action as half of the one defined in Eq. (29). In this appendix, we present the detailed calculations on the energy levels $E_n(x_c)$ within the WKB approximation, for the potential $V(x)$ defined as

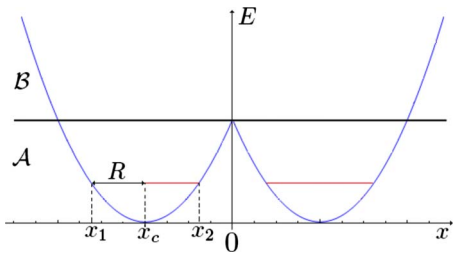

FIG. 22. (Color online) Double symmetric well. The two harmonic wells are centered in $\pm x_c$. The two turning points in the left well are x_1 and x_2, and R is the cyclotron radius.

$$V(x) = \begin{cases} \frac{1}{2}(x - x_c)^2 + \frac{V_0}{2} & \text{for } x \le 0 \\ \frac{1}{2}(x + x_c)^2 - \frac{V_0}{2} & \text{for } x \ge 0. \end{cases} \tag{A1}$$

The case $V_0=0$ has been introduced in Sec. III B for the study of edge states in zigzag nanoribbons while the case $V_0=1$ has been used in Sec. III C to describe armchair ribbons.

1. Double symmetric harmonic well

We consider the peculiar case $V_0=0$, that is a double symmetric harmonic potential,

$$V_{sym}(x) = \frac{1}{2}(|x| + x_c)^2. \tag{A2}$$

For a given energy E, we define the cyclotron radius as $R=\sqrt{2E}$ (Fig. 22). In addition, in the whole appendix, the factor 2 in the definition of the action [Eq. (29)] is missing: the actions S_l and S_r are now defined as the half of those introduced in Sec. IV.

a. Region $\mathcal{A}$: $R \le |x_c|$

This case, characterized by $E \le x_c^2/2$, corresponds to the region $\mathcal{A}$ in Fig. 22. We write the WKB wave functions in both wells and then the matching conditions in $x=0$. As the potential is symmetric with x, we focus on the left well ($x<0$). The energy E defines two classical turning points at positions $x_1=x_c-R$ and $x_l=x_c+R$ (Fig. 22). Within the WKB approximation, the connection procedure near x_1 implies that the wave function in the well reads

$$\varphi_l^{\leftarrow}(x) = \frac{C_l}{\sqrt{k(x)}} \sin\left[\mathcal{S}(x_1,x) + \frac{\pi}{4}\right], \tag{A3}$$

where the left arrow indicates that this wave function matches the correct connection procedure near the left turning point x_1. C_l is a constant and $\mathcal{S}(x_1,x)$ is the partial action in the left well,

$$\mathcal{S}(x_1,x) = \int_{x_1}^{x} dx \sqrt{E - V_{sym}(x)}. \tag{A4}$$

The above expression (A3) breaks down near the second turning point $x_l=x_c+R$. Near this point we linearize the potential as $V_{sym}(x) \approx \frac{R^2}{2} + R(x-x_l)$ and the Schrödinger equation reads

$$\left[\frac{d^2}{dx^2} - 2R(x - x_l)\right] \varphi^l(x) = 0. \tag{A5}$$

The solution of this equation is given by a combination of Airy functions,

$$\varphi_l^{\rightarrow}(x) = \bar{\alpha}_l \,\mathrm{Ai}(ax + x_0) + \bar{\beta}_l \,\mathrm{Bi}(ax + x_0), \tag{A6}$$

$$a^3 \equiv 2R, \tag{A7}$$

$$x_0 \equiv (2R)^{1/3}(R - |x_c|), \tag{A8}$$

where the right arrow indicates that this wave function must obey proper matching conditions near the right turning point x_l. $\bar{\alpha}_l$ and $\bar{\beta}_l$ are constants. Inside the well, this wave function has the asymptotic expansion,

$$\varphi_l^{\rightarrow}(x) \simeq \frac{\bar{\alpha}_l}{\sqrt{\pi}|z|^{1/4}} \sin\left(\frac{2}{3}|z|^{3/2} + \frac{\pi}{4}\right) + \frac{\bar{\beta}_l}{\sqrt{\pi}|z|^{1/4}} \cos\left(\frac{2}{3}|z|^{3/2} + \frac{\pi}{4}\right) \tag{A9}$$

with

$$|z| \equiv -x_0 - ax = \frac{k^2(x)}{a^2}. \tag{A10}$$

The argument in the trigonometric functions can be related to the partial action between x and x_l,

$$\frac{2}{3}|z|^{3/2} = \int_x^{x_l} dx \sqrt{E - V_{sym}(x)} = S_l - \mathcal{S}(x_1,x), \tag{A11}$$

where S_l is the total action in the left well. Therefore $\varphi_l^{\rightarrow}(x)$ can be rewritten in the form

$$\varphi_l^{\rightarrow}(x) \simeq \frac{\alpha_l}{\sqrt{k(x)}} \cos\left[\mathcal{S}(x_1,x) + \frac{\pi}{4} - S_l\right] + \frac{\beta_l}{\sqrt{k(x)}} \sin\left[\mathcal{S}(x_1,x) + \frac{\pi}{4} - S_l\right] \tag{A12}$$

with $\alpha_l = \bar{\alpha}_l\sqrt{\frac{a}{\pi}}$ (idem for β_l). Then, we impose $\varphi_l^{\leftarrow}(x) = \varphi_l^{\rightarrow}(x)$ inside the well. This implies $\alpha_l = C_l \sin S_l$ and $\beta_l = C_l \cos S_l$ what finally leads to the important relation

$$\tan S_l = \frac{\bar{\alpha}_l}{\bar{\beta}_l} = \frac{\alpha_l}{\beta_l}. \tag{A13}$$

As the two wells are identical, we obtain the same relation for the right well,

$$\tan S_r = \frac{\bar{\alpha}_r}{\bar{\beta}_r} = \frac{\alpha_r}{\beta_r} \tag{A14}$$

and similarly to Eq. (A6), the wave function in the right well reads near $x=0$,

$$\varphi_r^{\leftarrow}(x) = \bar{\alpha}_r \,\mathrm{Ai}(-ax + x_0) + \bar{\beta}_r \,\mathrm{Bi}(-ax + x_0). \quad \text{(A15)}$$

The next step is to impose the matching of the two wave functions and their derivatives in $x=0$,

$$\varphi_l^{\rightarrow}(0) = \varphi_r^{\leftarrow}(0), \quad \partial_x\varphi_l^{\rightarrow}(0) = \partial_x\varphi_r^{\leftarrow}(0). \quad \text{(A16)}$$

These matching conditions give the two equations,

$$\bar{\alpha}_l \,\mathrm{Ai}(x_0) + \bar{\beta}_l \,\mathrm{Bi}(x_0) = \bar{\alpha}_r \,\mathrm{Ai}(x_0) + \bar{\beta}_r \,\mathrm{Bi}(x_0),$$

$$\bar{\alpha}_l \,\mathrm{Ai}'(x_0) + \bar{\beta}_l \,\mathrm{Bi}'(x_0) = -\bar{\alpha}_r \,\mathrm{Ai}'(x_0) - \bar{\beta}_r \,\mathrm{Bi}'(x_0)$$

from which the ratio $\frac{\bar{\alpha}_r}{\bar{\beta}_r}$ is extracted as

$$\frac{\bar{\alpha}_r}{\bar{\beta}_r} = -\frac{\frac{\bar{\alpha}_l}{\bar{\beta}_l}[\mathrm{Bi}'(x_0)\mathrm{Ai}(x_0) + \mathrm{Bi}(x_0)\mathrm{Ai}'(x_0)] + 2\,\mathrm{Bi}'(x_0)\mathrm{Bi}(x_0)}{\frac{\bar{\alpha}_l}{\bar{\beta}_l} 2\,\mathrm{Ai}'(x_0)\mathrm{Ai}(x_0) + \mathrm{Ai}'(x_0)\mathrm{Bi}(x_0) + \mathrm{Ai}(x_0)\mathrm{Bi}'(x_0)}. \quad \text{(A17)}$$

The symmetry of the potential implies $S_l=S_r$ so that, from Eqs. (A13) and (A14), we have $\frac{\bar{\alpha}_r}{\bar{\beta}_r} = \frac{\bar{\alpha}_l}{\bar{\beta}_l} \equiv X$. The relation [Eq. (A17)] becomes a simple polynomial for the unknown quantity X,

$$\mathrm{Ai}'(x_0)\mathrm{Ai}(x_0)X^2 + [\mathrm{Ai}'(x_0)\mathrm{Bi}(x_0) + \mathrm{Ai}(x_0)\mathrm{Bi}'(x_0)]X + \mathrm{Bi}(x_0)\mathrm{Bi}'(x_0) = 0 \quad \text{(A18)}$$

whose solutions

$$X^S = -\frac{\mathrm{Bi}'(x_0)}{\mathrm{Ai}'(x_0)} \quad X^{AS} = -\frac{\mathrm{Bi}(x_0)}{\mathrm{Ai}(x_0)} \quad \text{(A19)}$$

Correspond, respectively, to the symmetric and antisymmetric wave functions. The action S_l is quantized by the condition $\tan S_l = X^{S,AS}$ so that $S_l = \pi(n+\gamma)$ with $0 \le \gamma < 1$, with two solutions for γ,

$$\gamma^S(E,x_c) = -\frac{1}{\pi}\arctan\frac{\mathrm{Bi}'(x_0)}{\mathrm{Ai}'(x_0)}, \quad \text{(A20)}$$

$$\gamma^{AS}(E,x_c) = 1 - \frac{1}{\pi}\arctan\frac{\mathrm{Bi}(x_0)}{\mathrm{Ai}(x_0)}. \quad \text{(A21)}$$

In region $\mathcal{A}$, the action is very simply related to the energy, $S_l = \pi R^2/2 = \pi E$ so that from Eqs. (A21), we obtain the implicit equations,

$$E_n^S = n + \frac{1}{\pi}\arctan\left[-\frac{\mathrm{Bi}'(x_0)}{\mathrm{Ai}'(x_0)}\right], \quad \text{(A22)}$$

$$E_n^{AS} = n + 1 + \frac{1}{\pi}\arctan\left[-\frac{\mathrm{Bi}(x_0)}{\mathrm{Ai}(x_0)}\right], \quad \text{(A23)}$$

where x_0 itself depends on the energy,

$$x_0 = (2\sqrt{2E_n})^{1/3}(\sqrt{2E_n} - |x_c|).$$

These implicit equations are solved numerically and we obtain the spectrum (region $\mathcal{A}$) shown in Fig. 23.

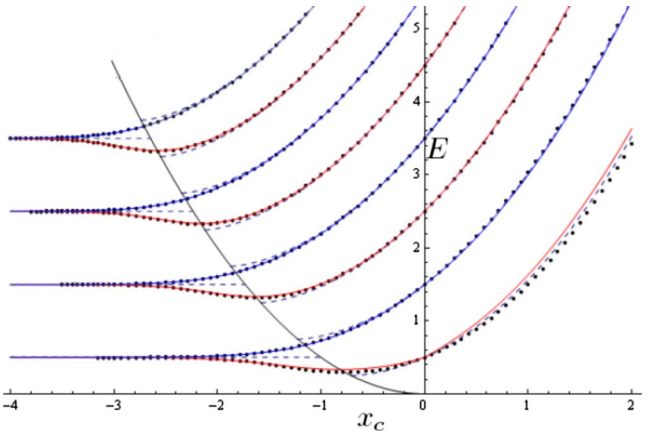

FIG. 23. (Color online) Semiclassical spectra $E_n(x_c)$ within the semiclassical approximation (dashed lines) $\gamma = cst$ and (full lines) WKB method. The dots are the exact numerical solutions of the Schrödinger equation with the potential $V_{sym}(x)$. The two regions are separated by the parabola $E = x_c^2/2$. For the zigzag problem, we keep only antisymmetric states that are the high-energy levels (blue lines).

b. Region $\mathcal{B}$: $|x_c| \le R$

This is the region $\mathcal{B}$ illustrated in Fig. 22. The expression of the WKB wave function matching the correct connection procedure near x_1 is still given by Eq. (A3). The second turning point in x_2 does not exist anymore, and we have to know the expression of the wave function near $x=0$. It reads

$$\varphi_l^{\rightarrow}(x) = \bar{\alpha}_l \,\mathrm{Ai}(y_0 + ax) + \bar{\beta}_l \,\mathrm{Bi}(y_0 + ax), \quad \text{(A24)}$$

$$a^3 \equiv 2|x_c|, \quad \text{(A25)}$$

$$y_0 \equiv \frac{x_c^2 - R^2}{(2|x_c|)^{2/3}}. \quad \text{(A26)}$$

Far from $x=0$, the Airy functions can be expanded to obtain

$$\varphi_l^{\rightarrow}(x) \simeq \frac{\bar{\alpha}_l}{\sqrt{\pi}|z|^{1/4}}\sin\left(\frac{2}{3}|z|^{3/2} + \frac{\pi}{4}\right) + \frac{\bar{\beta}_l}{\sqrt{\pi}|z|^{1/4}}\cos\left(\frac{2}{3}|z|^{3/2} + \frac{\pi}{4}\right),$$

where we have set

$$|z| \equiv -y_0 - ax = \frac{k^2(x)}{a^2}, \quad \alpha_l \equiv \frac{\bar{\alpha}_l}{\sqrt{\pi}}(2|x_c|)^{1/6}. \quad \text{(A27)}$$

The arguments in the trigonometric functions can be related to the partial action between x and 0,

$$\frac{2}{3}|z|^{3/2} = \int_x^0 dx\sqrt{R^2 - x_c^2 - 2|x_c|x} + \delta = S_l - \mathcal{S}(x_1,x) + \delta, \quad \text{(A28)}$$

where the quantity,

$$\delta \equiv \frac{(R^2 - x_c^2)^{3/2}}{3|x_c|} \tag{A29}$$

accounts for the step between the potential $V(x=0)$ and the energy E. The wave function $\varphi_l^{\rightarrow}(x)$ can thus be rewritten as

$$\varphi_l^{\rightarrow}(x) \simeq \frac{\alpha_l}{\sqrt{k(x)}}\cos\left[\mathcal{S}(x_1,x) + \frac{\pi}{4} - S_l - \delta\right] + \frac{\beta_l}{\sqrt{k(x)}}\sin\left[\mathcal{S}(x_1,x) + \frac{\pi}{4} - S_l - \delta\right]. \tag{A30}$$

The matching of the two wave functions $\varphi_l^{\leftarrow}(x) = \varphi_l^{\rightarrow}(x)$ gives

$$\tan(S_l + \delta) = \frac{\alpha_l}{\beta_l} \tag{A31}$$

and a similar expression for the right well. Again we impose the continuity of the wave function and its derivative in $x=0$ and obtain the two equations:

$$\bar{\alpha}_l\,\mathrm{Ai}(y_0) + \bar{\beta}_l\,\mathrm{Bi}(y_0) = \bar{\alpha}_r\,\mathrm{Ai}(y_0) + \bar{\beta}_r\,\mathrm{Bi}(y_0),$$

$$\bar{\alpha}_l\,\mathrm{Ai}'(y_0) + \bar{\beta}_l\,\mathrm{Bi}'(y_0) = -\bar{\alpha}_r\,\mathrm{Ai}'(y_0) - \bar{\beta}_r\,\mathrm{Bi}'(y_0)$$

from where we extract the ratio α_r/β_r. Then, using the symmetry $\alpha_l=\alpha_r$ and $\beta_l=\beta_r$, we obtain a polynomial in $X \equiv \alpha_l/\beta_l$,

$$\mathrm{Ai}'(y_0)\mathrm{Ai}(y_0)X^2 + [\mathrm{Ai}'(y_0)\mathrm{Bi}(y_0) + \mathrm{Ai}(y_0)\mathrm{Bi}'(y_0)]X + \mathrm{Bi}(y_0)\mathrm{Bi}'(y_0) = 0. \tag{A32}$$

The only difference with the polynomial [Eq. (A18)] for the region $\mathcal{A}$ consists in the substitution $x_0 \to y_0$. Consequently, the solutions are

$$X^S = -\frac{\mathrm{Bi}'(y_0)}{\mathrm{Ai}'(y_0)} \quad X^{AS} = -\frac{\mathrm{Bi}(y_0)}{\mathrm{Ai}(y_0)}. \tag{A33}$$

The action S_l is quantized by the condition $\tan S_l = X^{S,AS}$ so that $S_l = \pi(n+\gamma)$ with $0 \le \gamma < 1$, with two solutions for γ,

$$\gamma^{S,AS}(E,x_c) = \sigma\left[\frac{1}{\pi}(\arctan X^{S,AS} - \delta)\right], \tag{A34}$$

where $\sigma(x) = x - [x]$, $[x]$ being the next smallest integer. By construction $0 \le \sigma[x] < 1$.

The last step is to relate the energy to the action. This relation is not linear as in region $\mathcal{A}$ but it now reads [see Eq. (32)],

$$S_l = E\left(\theta - \frac{1}{2}\sin 2\theta\right), \tag{A35}$$

where $\theta = \arccos x_c/R = \arccos x_c/\sqrt{2E}$ has the meaning of a angle (Sec. V). From this equation, together with the quantization condition,

$$S_l = \pi(n + \gamma^{S,AS}), \tag{A36}$$

where $\gamma^{S,AS}(E,x_c)$ are functions of E and x_c through Eqs. (A26), we can extract numerically the eigenenergies E_n^S and E_n^{AS} and plot them as a function of x_c in Fig. 23. In Fig. 24 we have also plotted the x_c dependence of the mismatch index $\gamma^{S,AS}(x_c)$.

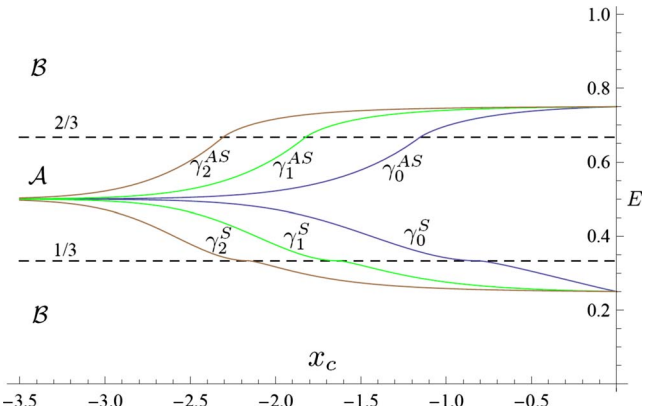

FIG. 24. (Color online) Mismatch index $\gamma^{S,AS}(x_c)$ as a function of x_c, for (blue) $n=0$, (green) $n=1$, and (brown) $n=2$. For $x_c=R$, $\gamma^S(R)=1/3$ whereas $\gamma^{AS}(R)=2/3$ (horizontal dashed lines). For $x_c=0$, $\gamma^S(0)=1/4$, and $\gamma^{AS}(0)=3/4$.

2. Double harmonic asymmetric well

In this section we introduce an asymmetry $V_0=1$ in the potential which becomes

$$V_{asym}(x) = \begin{cases} \frac{1}{2}(x-x_c)^2 + \frac{1}{2} & \text{for } x \le 0 \\ \frac{1}{2}(x+x_c)^2 - \frac{1}{2} & \text{for } x \ge 0 \end{cases} \tag{A37}$$

and calculate the spectrum $E_n(x_c)$ within the WKB approximation. We now introduce two cyclotron radii R_l and R_r. The relation between these parameters and the classical energy is given by

$$E = \frac{R_l^2 + 1}{2} = \frac{R_r^2 - 1}{2}. \tag{A38}$$

We now have to distinguish three regions delimited by $|x_c| = R_l$ and $|x_c| = R_r$ and illustrated in Fig. 25. The total action in these three regions reads

$$\text{region } \mathcal{C} \quad S_t = \frac{\pi}{2}R_l^2 + \frac{\pi}{2}R_r^2,$$

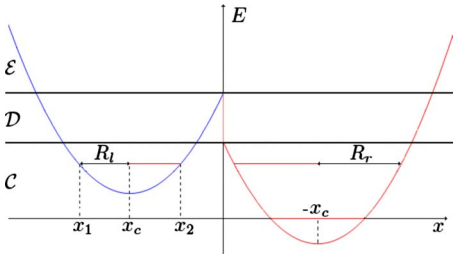

FIG. 25. (Color online) Double asymmetric well $V_{asym}(x)$: $\mathcal{C}$, $\mathcal{D}$, and $\mathcal{E}$ refer to the three regions discussed in the text. For a given energy E, we define two cyclotron radii R_l and R_r.

region $\mathcal{D}$ $S_t = \frac{\pi}{2}R_l^2 + \frac{R_r^2}{2}\left[\theta_r - \frac{1}{2}\sin(2\theta_r)\right]$,

region $\mathcal{E}$ $S_t = \frac{R_l^2}{2}\left[\theta_l - \frac{1}{2}\sin(2\theta_l)\right] + \frac{R_r^2}{2}\left[\theta_r - \frac{1}{2}\sin(2\theta_r)\right]$. (A39)

We treat the three regions separately.

3. Region $\mathcal{C}$: $R_l \leq R_r \leq |x_c|$

This region is explicited in Fig. 25. Because of the asymmetry of the potential, the action is now different in each well,

$$S_l = \frac{\pi}{2}R_l^2 = \pi(E - 1/2), \tag{A40}$$

$$S_r = \frac{\pi}{2}R_r^2 = \pi(E + 1/2). \tag{A41}$$

The WKB wave function has the same form as in Eqs. (A3), (A6), and (A9) written for the symmetric potential so that we still have the relations [Eqs. (A13) and (A14)]. Since the potential is now asymmetric, the expression of the wave function near the two inner turning points located in $-|x_c|+R_l$ and $|x_c|-R_r$ is now

$$\varphi_l^{\rightarrow}(x) = \bar{\alpha}_l \,\mathrm{Ai}(a_l x + x_l) + \bar{\beta}_l \,\mathrm{Bi}(a_l x + x_l) \tag{A42}$$

$$\varphi_r^{\leftarrow}(x) = \bar{\alpha}_r \,\mathrm{Ai}(-a_r x + x_r) + \bar{\beta}_l \,\mathrm{Bi}(-a_r x + x_r) \tag{A43}$$

with

$$a_l^3 \equiv 2R_l \quad a_r^3 \equiv 2R_r, \tag{A44}$$

$$x_l \equiv (2R_l)^{1/3}(R_l - |x_c|), \tag{A45}$$

$$x_r \equiv (2R_r)^{1/3}(R_r - |x_c|). \tag{A46}$$

Then, by imposing the current conservation and the continuity of these wave functions in $x=0$, we obtain the two equations,

$$\bar{\alpha}_l \,\mathrm{Ai}(x_l) + \bar{\beta}_l \,\mathrm{Bi}(x_l) = \bar{\alpha}_r \,\mathrm{Ai}(x_r) + \bar{\beta}_r \,\mathrm{Bi}(x_r)$$

$$\bar{\alpha}_l a_l \,\mathrm{Ai}'(x_l) + \bar{\beta}_l a_l \,\mathrm{Bi}'(x_l) = -\bar{\alpha}_r a_r \,\mathrm{Ai}'(x_r) - \bar{\beta}_r a_r \,\mathrm{Bi}'(x_r) \tag{A47}$$

from where we extract the ratio $\frac{\bar{\alpha}_r}{\bar{\beta}_r}$ as

$$\frac{\bar{\alpha}_r}{\bar{\beta}_r} = -\frac{\frac{\bar{\alpha}_l}{\bar{\beta}_l}\left[\mathrm{Bi}'(x_r)\mathrm{Ai}(x_l) + \mathrm{Bi}(x_r)\mathrm{Ai}'(x_l)\left(\frac{R_l}{R_r}\right)^{1/3}\right] + \mathrm{Bi}'(x_r)\mathrm{Bi}(x_l) + \mathrm{Bi}(x_r)\mathrm{Bi}'(x_l)\left(\frac{R_l}{R_r}\right)^{1/3}}{\frac{\bar{\alpha}_l}{\bar{\beta}_l}\left[\mathrm{Ai}'(x_r)\mathrm{Ai}(x_l) + \mathrm{Ai}(x_r)\mathrm{Ai}'(x_l)\left(\frac{R_l}{R_r}\right)^{1/3}\right] + \mathrm{Ai}'(x_r)\mathrm{Bi}(x_l) + \mathrm{Ai}(x_r)\mathrm{Bi}'(x_l)\left(\frac{R_l}{R_r}\right)^{1/3}}. \tag{A48}$$

Since $S_l \neq S_r$, the ratios $\frac{\bar{\alpha}_r}{\bar{\beta}_r}$ and $\frac{\bar{\alpha}_l}{\bar{\beta}_l}$ are now different. Introducing the total action $S_t = S_r + S_l = 2\pi E$, these coefficients are related as

$$\frac{\alpha_r}{\beta_r} = \frac{\tan S_t - \alpha_l/\beta_l}{1 + \alpha_l/\beta_l \tan S_t}. \tag{A49}$$

Then, we insert the relation Eq. (A49) into Eq. (A48) to obtain a polynomial in $X_l \equiv \alpha_l/\beta_l$ whose the coefficients are only functions of E and x_c,

$$\left\{\tan S_t\left[\mathrm{Bi}'(x_r)\mathrm{Ai}(x_l) + \left(\frac{R_l}{R_r}\right)^{1/3}\mathrm{Bi}(x_r)\mathrm{Ai}'(x_l)\right] - \mathrm{Ai}'(x_r)\mathrm{Ai}(x_l) - \left(\frac{R_l}{R_r}\right)^{1/3}\mathrm{Ai}'(x_l)\mathrm{Ai}(x_r)\right\}X_l^2,$$

$$\left\{\tan S_t\left\{\mathrm{Ai}'(x_r)\mathrm{Ai}(x_l) + \mathrm{Bi}'(x_r)\mathrm{Bi}(x_l) + \left(\frac{R_l}{R_r}\right)^{1/3}[\mathrm{Ai}'(x_l)\mathrm{Ai}(x_r) + \mathrm{Bi}'(x_r)\mathrm{Bi}(x_l)]\right\}\right.$$
$$\left. + \mathrm{Bi}'(x_r)\mathrm{Ai}(x_l) - \mathrm{Ai}'(x_r)\mathrm{Bi}(x_l) + \left(\frac{R_l}{R_r}\right)^{1/3}[\mathrm{Bi}(x_r)\mathrm{Ai}'(x_l) - \mathrm{Ai}(x_r)\mathrm{Bi}'(x_l)]\right\}X_l$$

$$\tan S_t\left[\mathrm{Ai}'(x_r)\mathrm{Bi}(x_l) + \left(\frac{R_l}{R_r}\right)^{1/3}\mathrm{Ai}(x_r)\mathrm{Bi}'(x_l)\right] + \mathrm{Bi}'(x_r)\mathrm{Bi}(x_l) + \left(\frac{R_l}{R_r}\right)^{1/3}\mathrm{Bi}(x_r)\mathrm{Bi}'(x_l) = 0 \tag{A50}$$

with $S_t=2\pi E$. Because of the asymmetry of the potential, the coefficients of the polynomial are much more complicated than for the symmetric case [Eq. (A18)]. We check that for $R_r=R_l$ and $x_l=x_r=x_0$ we recover the symmetric case [Eq. (A18)]. The polynomial [Eq. (A50)] has still two solutions X_l^S and X_l^{AS}, from which we obtain the action S_l. It has the from $S_l=\pi(n+\gamma)$ with

$$\gamma_l^S(E,x_c)=\frac{1}{\pi}\arctan X_l^S, \tag{A51}$$

$$\gamma_l^{AS}(E,x_c)=\frac{1}{\pi}\arctan X_l^{AS}+1. \tag{A52}$$

Since the energy E is simply related to the action $E=1/2+S_l/\pi$, we finally obtain the two implicit equations,

$$E_n^S=n+\frac{1}{2}+\frac{1}{\pi}\arctan X_l^S, \tag{A53}$$

$$E_n^{AS}=n+\frac{3}{2}-\frac{1}{\pi}\arctan X_l^{AS} \tag{A54}$$

from which we obtain the energy levels $E_n(x_c)$ in the region $R_l\leq R_r\leq|x_c|$.

4. Region $\mathcal{D}$: $R_l\leq|x_c|\leq R_r$

The region $\mathcal{D}$ represented in Fig. 25 does not exist for the symmetric potential $V_{sym}(x)$. We have now to linearize the potential around $-|x_c|+R_l$ for the left well and around $x=0$ for the right well. The solution inside the left well takes the familiar form

$$\Psi^l(x)=\bar{\alpha}_l\,\mathrm{Ai}(a_lx+x_l)+\bar{\beta}_l\,\mathrm{Bi}(a_lx+x_l), \tag{A55}$$

$$a_l^3=2R_l, \tag{A56}$$

$$x_l=(2R_l)^{1/3}(R_l-|x_c|), \tag{A57}$$

whereas the one inside the right well is

$$\Psi^r(x)=\bar{\alpha}_r\,\mathrm{Ai}(y_r-a_rx)+\bar{\beta}_r\,\mathrm{Bi}(y_r-a_rx), \tag{A58}$$

$$a_r^3=|2x_c|, \tag{A59}$$

$$y_r=\frac{x_c^2-R_r^2}{|2x_c|^{2/3}}. \tag{A60}$$

The next step consists in the matching of the Airy functions with the WKB approximation valuable inside a well. The treatment for the left well has been performed in the paragraph a, of this appendix and gives

$$\tan S_l=\frac{\alpha_l}{\beta_l}=\frac{\bar{\alpha}_l}{\bar{\beta}_l}, \tag{A61}$$

whereas the calculation for the right well has been made in the paragraph b and gives

$$\tan(S_r+\delta_r)=\frac{\alpha_r}{\beta_r}=\frac{\bar{\alpha}_r}{\bar{\beta}_r}, \tag{A62}$$

where

$$\delta_r=\frac{(R_r^2-x_c^2)^{3/2}}{3|x_c|}. \tag{A63}$$

The current conservation and the continuity of the wave function at $x=0$ gives the two equations,

$$\bar{\alpha}_l\,\mathrm{Ai}(x_l)+\bar{\beta}_l\,\mathrm{Bi}(x_l)=\bar{\alpha}_r\,\mathrm{Ai}(y_r)+\bar{\beta}_r\,\mathrm{Bi}(y_r),$$

$$\bar{\alpha}_la_l\,\mathrm{Ai}'(x_l)+\bar{\beta}_la_l\,\mathrm{Bi}'(x_l)=-\bar{\alpha}_ra_r\,\mathrm{Ai}'(y_r)-\bar{\beta}_ra_r\,\mathrm{Bi}'(y_r)$$

from where we extract the ratio $\frac{\bar{\alpha}_r}{\bar{\beta}_r}$,

$$\frac{\bar{\alpha}_r}{\bar{\beta}_r}=-\frac{\frac{\bar{\alpha}_l}{\bar{\beta}_l}\left[\mathrm{Bi}'(y_r)\mathrm{Ai}(x_l)+\left(\frac{R_l}{|x_c|}\right)^{1/3}\mathrm{Bi}(y_r)\mathrm{Ai}'(x_l)\right]+\mathrm{Bi}'(y_r)\mathrm{Bi}(x_l)+\left(\frac{R_l}{|x_c|}\right)^{1/3}\mathrm{Bi}(y_r)\mathrm{Bi}'(x_l)}{\frac{\bar{\alpha}_l}{\bar{\beta}_l}\left[\mathrm{Ai}'(y_r)\mathrm{Ai}(x_l)+\left(\frac{R_l}{|x_c|}\right)^{1/3}\mathrm{Ai}(y_r)\mathrm{Ai}'(x_l)\right]+\mathrm{Ai}'(y_r)\mathrm{Bi}(x_l)+\left(\frac{R_l}{|x_c|}\right)^{1/3}\mathrm{Ai}(y_r)\mathrm{Bi}'(x_l)}. \tag{A64}$$

Introducing the total action $S_t=S_l+S_r$ and using Eqs. (A61) and (A62) we obtain the relation,

$$\frac{\alpha_r}{\beta_r}=\frac{\tan(S_t+\delta_r)-\frac{\alpha_l}{\beta_l}}{1+\tan(S_t+\delta_r)\frac{\alpha_l}{\beta_l}}=\frac{\nu-X_l}{1+\nu X_l}, \tag{A65}$$

where we have introduced $\nu\equiv\tan(S_t+\delta_r)$. We inject this last relation into Eq. (A64) to obtain again a polynomial in X_l,

$$\left\{\nu\left[\mathrm{Bi}'(y_r)\mathrm{Ai}(x_l)+\left(\frac{R_l}{|x_c|}\right)^{1/3}\mathrm{Bi}(y_r)\mathrm{Ai}'(x_l)\right]-\mathrm{Ai}'(y_r)\mathrm{Ai}(x_l)-\left(\frac{R_l}{|x_c|}\right)^{1/3}\mathrm{Ai}'(x_l)\mathrm{Ai}(y_r)\right\}X_l^2$$
$$+\left\{\nu\left\{\mathrm{Ai}'(y_r)\mathrm{Ai}(x_l)+\mathrm{Bi}'(y_r)\mathrm{Bi}(x_l)+\left(\frac{R_l}{|x_c|}\right)^{1/3}[\mathrm{Ai}'(x_l)\mathrm{Ai}(y_r)+\mathrm{Bi}'(x_l)\mathrm{Bi}(y_r)]\right\}+\mathrm{Bi}'(y_r)\mathrm{Ai}(x_l)-\mathrm{Ai}'(y_r)\mathrm{Bi}(x_l)\right.$$
$$\left.+\left(\frac{R_l}{|x_c|}\right)^{1/3}[\mathrm{Bi}(y_r)\mathrm{Ai}'(x_l)-\mathrm{Ai}(y_r)\mathrm{Bi}'(x_l)]\right\}X_l+\nu\left[\mathrm{Ai}'(y_r)\mathrm{Bi}(x_l)+\left(\frac{R_l}{|x_c|}\right)^{1/3}\mathrm{Ai}(y_r)\mathrm{Bi}'(x_l)\right]+\mathrm{Bi}'(y_r)\mathrm{Bi}(x_l)$$
$$+\left(\frac{R_l}{|x_c|}\right)^{1/3}\mathrm{Bi}(y_r)\mathrm{Bi}'(x_l)=0. \tag{A66}$$

Note that this polynomial satisfies the continuity of the spectrum on the parabola for which $x_c=R_r$. Indeed, in this case we have $\delta_r=0$ and $x_r=y_r=0$ so that the two polynomials [Eq. (A50)] in region $\mathcal{C}$ and Eq. (A66) in region $\mathcal{D}$ coincide and give the same solutions. From here, the work is exactly the same than for the lower region. Therefore, we have just to take the two solutions X_l^S and X_l^{AS} of this polynomial and insert them into Eq. (A51) to obtain the left mismatch index in the intermediate region. Then we insert them into Eqs. (A53) and (A54) to obtain the implicit equations in E_n and x_c from where we can extract the spectrum $E_n(x_c)$ in the region $\mathcal{D}$, characterized by the relation $R_l\leq|x_c|\leq R_r$.

5. Region $\mathcal{E}$: $|x_c|\leq R_l\leq R_r$

The last region $\mathcal{E}$ satisfies $|x_c|\leq R_l\leq R_r$ and is illustrated in Fig. 25. As for the high-energy region of the double symmetric well, we decompose the well into two parts from $x=0$, and keep working with S_l that is the action in the well where $x<0$. The strategy is still the same, and the calculations are very similar to those in Appendix A 1 b. We express the ratio α/β from two ways. First, we obtain a relation of the type [Eq. (A31)] thanks to the matching of the WKB wave function with the solutions of the linearized Schrödinger equation around $x=0$ that we express as

$$\Psi^l(x)=\bar{\alpha}_l\,\mathrm{Ai}(a_l x+y_l)+\bar{\beta}_l\,\mathrm{Bi}(a_l x+y_l)\quad\text{for } x<0,$$

$$\Psi^r(x)=\bar{\alpha}_r\,\mathrm{Ai}(y_r-a_r x)+\bar{\beta}_r\,\mathrm{Bi}(y_r-a_r x)\quad\text{for } x>0,$$

$$y_l=\frac{x_c^2-R_l^2}{|2x_c|^{2/3}}\quad y_r=\frac{x_c^2-R_r^2}{|2x_c|^{2/3}},$$

$$a_l^3=a_r^3=|2x_c|.$$

The difference here comes from the asymmetry $V_0=1$ so that the relation [Eq. (A31)] becomes

$$\tan(S_l+\delta_l)=X_l=\frac{\alpha_l}{\beta_l}, \tag{A67}$$

$$\tan(S_r+\delta_r)=X_r=\frac{\alpha_r}{\beta_r}, \tag{A68}$$

$$\delta_r=\frac{(R_r^2-x_c^2)^{3/2}}{3|x_c|}\quad\delta_l=\frac{(R_l^2-x_c^2)^{3/2}}{3|x_c|} \tag{A69}$$

In order to obtain a polynomial in terms of X_l in the high-energy region, we use the latest relations to express X_r as a function of X_l,

$$X_r=\frac{\tan(S_t+\delta_r)-\tan S_l}{1+\tan S_l\tan(S_t+\delta_r)}=\frac{(\nu\tan\delta_l-1)\dfrac{\alpha_l}{\beta_l}+\nu+\tan\delta_l}{(\nu+\tan\delta_l)\dfrac{\alpha_l}{\beta_l}-(\nu\tan\delta_l-1)},$$

$$X_r=\frac{\sigma X_l+\tau}{\tau X_l-\sigma}, \tag{A70}$$

where we have introduced $\sigma\equiv\nu\tan\delta_l-1$ and $\tau\equiv\nu+\tan\delta_l$. Then, we use the continuity conditions at $x=0$ to obtain

$$X_r=\frac{\bar{\alpha}_r}{\bar{\beta}_r}=-\frac{X_l[\mathrm{Bi}'(y_r)\mathrm{Ai}(y_l)+\mathrm{Bi}(y_r)\mathrm{Ai}'(y_l)]+\mathrm{Bi}'(y_r)\mathrm{Bi}(y_l)+\mathrm{Bi}(y_r)\mathrm{Bi}'(y_l)}{X_l[\mathrm{Ai}'(y_r)\mathrm{Ai}(y_l)+\mathrm{Ai}(y_r)\mathrm{Ai}'(y_l)]+\mathrm{Ai}'(y_r)\mathrm{Bi}(y_l)+\mathrm{Ai}(y_r)\mathrm{Bi}'(y_l)} \tag{A71}$$

From Eqs. (A70) and (A71), we obtain a polynomial for X_l,

$$\{\tau[\mathrm{Bi}'(y_r)\mathrm{Ai}(y_l)+\mathrm{Bi}(y_r)\mathrm{Ai}'(y_l)]+\sigma[\mathrm{Ai}'(y_r)\mathrm{Ai}(y_l)+\mathrm{Ai}'(y_l)\mathrm{Ai}(y_r)]\}X_l^2$$
$$+\{\tau[\mathrm{Ai}'(y_r)\mathrm{Ai}(y_l)+\mathrm{Bi}'(y_r)\mathrm{Bi}(y_l)+\mathrm{Ai}'(y_l)\mathrm{Ai}(y_r)+\mathrm{Bi}'(y_l)\mathrm{Bi}(y_r)]$$
$$-\sigma[\mathrm{Bi}'(y_r)\mathrm{Ai}(y_l)-\mathrm{Ai}'(y_r)\mathrm{Bi}(y_l)+\mathrm{Bi}(y_r)\mathrm{Ai}'(y_l)-\mathrm{Ai}(y_r)\mathrm{Bi}'(y_l)]\}X_l$$
$$+\tau[\mathrm{Ai}'(y_r)\mathrm{Bi}(y_l)+\mathrm{Ai}(y_r)\mathrm{Bi}'(y_l)]-\sigma[\mathrm{Bi}'(y_r)\mathrm{Bi}(y_l)+\mathrm{Bi}(y_r)\mathrm{Bi}'(y_l)]=0 \tag{A72}$$

Again, it is easy to check that for $|x_c|=R_l$, we have $\tau=\nu$, $\sigma=-1$, and $x_l=y_l=0$ so that the polynomials (Appendix A 1 b) in region $\mathcal{D}$ and Eq. (A72) in region $\mathcal{E}$ coincide, what assures the continuity of the spectrum between these two regions. To obtain the implicit equations and extract the spectrum $E_n(x_c)$ in this region, we inject the solutions $X^{S/AS}$ into Eq. (A67) to obtain an expression of the mismatch indices $\gamma^{S/AS}$ like in region $\mathcal{B}$ [see Eq. (A34) with $\delta \to \delta_l$] and write explicitly the action S_l as a function of the energy and x_c as in expression (32) with $R \to R_l$.

[1] P. R. Wallace, Phys. Rev. **71**, 622 (1947).
[2] K. S. Novoselov, A. K. Geim, S. V. Morozov, D. Jiang, M. I. Katsnelson, I. V. Grigorieva, S. V. Dubonos, and A. A. Firsov, Nature (London) **438**, 197 (2005).
[3] Y. Zhang, J. W. Tan, H. L. Stormer, and P. Kim, Nature (London) **438**, 201 (2005).
[4] A. Geim and K. Novoselov, Nature Mater. **6**, 183 (2007).
[5] Y.-W. Son, M. L. Cohen, and S. G. Louie, Nature (London) **444**, 347 (2006).
[6] M. Fujita, K. Wakabayashi, K. Nakada, and K. Kusakabe, J. Phys. Soc. Jpn. **65**, 1920 (1996).
[7] K. Nakada, M. Fujita, G. Dresselhaus, and M. S. Dresselhaus, Phys. Rev. B **54**, 17954 (1996).
[8] L. Brey and H. A. Fertig, Phys. Rev. B **73**, 235411 (2006).
[9] W. Yao, S. A. Yang, and Q. Niu, Phys. Rev. Lett. **102**, 096801 (2009).
[10] J. Klos, arXiv:0902.0914 (unpublished).
[11] W. Li and R. Tao, arXiv:1001.4168 (unpublished).
[12] B. Xu, J. Yin, H. Weng, Y. Xia, X. Wan, and Z. Liu, arXiv:1004.3465 (unpublished).
[13] A. R. Akhmerov and C. W. J. Beenakker, Phys. Rev. B **77**, 085423 (2008).
[14] S. Ihnatsenka, I. V. Zozoulenko, and G. Kirczenow, Phys. Rev. B **80**, 155415 (2009).
[15] J. Wurm, M. Wimmer, I. Adagideli, K. Richter, and H. U. Baranger, New J. Phys. **11**, 095022 (2009).
[16] Y. Kobayashi, K. I. Fukui, T. Enoki, K. Kusakabe, and Y. Kaburagi, Phys. Rev. B **71**, 193406 (2005).
[17] A. Chuvilin, J. C. Meyer, G. Algara-Siller, and U. Kaiser, New J. Phys. **11**, 083019 (2009).
[18] P. Koskinen, S. Malola, and H. Häkkinen, Phys. Rev. B **80**, 073401 (2009).
[19] M. Y. Han, J. C. Brant, and P. Kim, Phys. Rev. Lett. **104**, 056801 (2010).
[20] P. Gallagher, K. Todd, and D. Goldhaber-Gordon, Phys. Rev. B **81**, 115409 (2010).
[21] L. Brey and H. A. Fertig, Phys. Rev. B **73**, 195408 (2006).
[22] N. M. R. Peres, A. H. Castro Neto, and F. Guinea, Phys. Rev. B **73**, 241403 (2006).
[23] D. A. Abanin, P. A. Lee, and L. S. Levitov, Phys. Rev. Lett. **96**, 176803 (2006); Solid State Commun. **143**, 77 (2007).
[24] B. I. Halperin, Phys. Rev. B **25**, 2185 (1982); see also L. A. Fal'kovskii, Sov. Phys. JETP **31**(5), 981-987 (1970).
[25] M. Büttiker, Phys. Rev. B **38**, 9375 (1988).
[26] D. A. Bahamon, A. L. C. Pereira, and P. A. Schulz, Phys. Rev. B **79**, 125414 (2009).
[27] H. P. Dahal, Z.-X. Hu, N. A. Sinitsyn, K. Yang, and A. V. Balatsky, Phys. Rev. B **81**, 155406 (2010).
[28] V. P. Gusynin, V. A. Miransky, S. G. Sharapov, and I. A. Shovkovy, Phys. Rev. B **77**, 205409 (2008).
[29] S. Ryu and Y. Hatsugai, Phys. Rev. Lett. **89**, 077002 (2002).
[30] J. W. McClure, Phys. Rev. **104**, 666 (1956).
[31] Y. Avishai and G. Montambaux, Eur. Phys. J. B **66**, 41 (2008).
[32] H. van Houten, C. W. J. Beenakker, J. G. Williamson, M. E. I. Broekaart, P. H. M. van Loosdrecht, B. J. van Wees, J. E. Mooij, C. T. Foxon, and J. J. Harris, Phys. Rev. B **39**, 8556 (1989); H. van Houten and C. W. J. Beenakker, in *Analogies in Optics and Micro Electronics*, edited by W. van Haeringen and D. Lenstra (Kluwer, Dordrecht, 1990) p. 203-225; C. W. J. Beenakker, H. van Houten, and B. J. van Wees, Superlattices Microstruct. **5**, 127 (1989).
[33] G. Montambaux, arXiv:1006.5819 (unpublished).
[34] T. Matsui, H. Kambara, Y. Niimi, K. Tagami, M. Tsukada, and H. Fukuyama, Phys. Rev. Lett. **94**, 226403 (2005).
[35] Y. Niimi, T. Matsui, H. Kambara, K. Tagami, M. Tsukada, and H. Fukuyama, Phys. Rev. B **73**, 085421 (2006).
[36] Y. Niimi, H. Kambara, T. Matsui, D. Yoshioka, and H. Fukuyama, Phys. Rev. Lett. **97**, 236804 (2006).
[37] P. Rakyta, A. Kormanyos, J. Cserti, and P. Koskinen, Phys. Rev. B **81**, 115411 (2010).